Solar Energy 268 (2024) 112117

Contents lists available at ScienceDirect

Solar Energy

journal homepage: www.elsevier.com/locate/solener

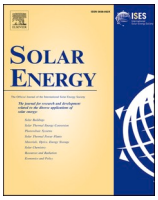

A falling particle receiver thermal model for system-level analysis of solar tower plants

Omar Pasqualotto, Filip Sobic *, Giancarlo Gentile, Marco Binotti, Andrea Giostri, Giampaolo Manzolini

Politecnico di Milano, Department of Energy, via Lambruschini 4A, 20156 Milan, Italy

ARTICLE INFO

Keywords:
Particle receiver
Solar tower
Thermal model
System-level
Optimization
Multi-stage

ABSTRACT

Falling particle receivers are one of the most promising new generation solar tower technologies. They have the advantage of being directly heated, thus relaxing flux limitations associated with conventional receivers, and being able to achieve very high temperatures (>1000 °C) without degradation. The goal of this work is the development of a thermal model able to describe the behaviour of a falling particle receiver under different operating conditions, to provide the value of its thermal efficiency within reasonable computational time so that the model can be applied for optimization of solar tower plants at system-level. The thermal model was developed starting from models described in literature, upgrading them with various features (e.g., 2D/3D discretization, drag force effect, etc.) to describe more in detail the heat transfer phenomena occurring during receiver operation. The obtained model results were verified against CFD showing better agreement than the original model. Furthermore, the thermal model was employed in a case study with the goal of optimizing the receiver size for a given solar field and performing off-design and annual performance analyses. Results showed that the adoption of multiple stages increases performance compared to a free-falling particle receiver both under nominal and off-design conditions, and the higher the number of stages the better is the performance. A free-falling particle receiver showed a yearly thermal efficiency of 72.0 %, while the five stages one achieved 75.3 %. In addition, recirculation was investigated as part load strategy for improving performance of the free-falling receiver, but the benefits in terms of performance were limited.

1. Introduction

In the last few decades, climate and environmental concerns have raised the issue of finding energy production technologies that could compete with fossil fuel-based ones while improving the sustainability of the energy sector and decreasing its carbon footprint [1,2].

In the "Gen3 Roadmap" published in 2017 by Sandia National Laboratories (SNL), Mehos et al. [3] introduced the three most interesting Solar Tower (ST) technology pathways on which the research effort should be focused on (i.e., molten salts, falling particle, gas phase). Following an extensive analysis of those three technologies carried out in the frame of the Generation 3 CSP Systems funding program, the U.S. Department of Energy announced in 2021 that the most promising pathway to achieve higher temperatures in CSP plants and to meet 2030 cost targets [4] is the one based on Particle Receiver (PR) [5].

In detail, the concept is to adopt particles as a heat transfer medium (HTM) instead of liquid fluids; this leads to some advantages including: i) the possibility of HTM direct heating that allows achievement of high temperatures, and ii) the possibility of cheaper Thermal Energy Storage (TES) because heat can be stored in a relatively inexpensive medium (e.g. sand) [3,6]).

More precisely, the adoption of direct heating allows avoiding the exposure of metallic tubes to the direct solar radiation allowing achievement of high temperatures and this leads in turn to the possibility of adopting power cycles with higher efficiencies than the ones adopted for conventional molten salts receivers.

Ho [6] provides a literature review of the different PR concepts, identifying the falling particle receiver as one of the most promising options. To fully understand falling particle receivers' performance and how to optimize plant design and operation it is thus necessary to develop a reliable receiver thermal model.

Regarding falling particle receiver models present in literature, Jiang et al. [7] used numerical model which is composed of an optical model as well as flow and heat transfer ones. To avoid computational burden of following multiple reflections of each sun ray inside the receiver, Monte

* Corresponding author.
E-mail address: filip.sobic@polimi.it (F. Sobic).

https://doi.org/10.1016/j.solener.2023.112117
Received 2 December 2022; Received in revised form 20 September 2023; Accepted 12 October 2023
Available online 5 January 2024

Nomenclature

Symbols

a	drag model correction factor
b	drag model multiplier coefficient
c_p	particle specific heat (kJ/kgK)
d_p	particle diameter (m)
F	view factor
F_{eq}	equivalent view factor
g	gravitational acceleration (m/s^2)
h_{adv}	advective heat transfer coefficient (W/m^{2}K)
$h_{aperture}$	aperture height (m)
h_{conv}	convective heat transfer coefficient (W/m^{2}K)
$h_{curtain}$	curtain height (m)
$h_{optical,tower}$	tower optical height (m)
h_{lift}	elevator height (m)
$h_{heliostat}$	heliostat height (m)
K_1	correction factor first coefficient
K_2	correction factor second coefficient
$\dot{m}_p^{'}$	lineic particle mass flow rate (kg/s/m)
Pr	Prandtl number
Ra	Rayleigh number
$\dot{Q}$	thermal power (W)
q	thermal flux (W/m^2)
Re	Reynolds number
t	thickness (m)
T	temperature (K)
v_{air}	air velocity (m/s)
v_p	particle velocity (m/s)
v_0	particle initial velocity (m/s)
w_c	curtain width (m)
x	width coordinate (m)
y	falling coordinate (m)
$\tilde{y}$	vertical wall coordinate (m)
z	thickness coordinate (m)

Greek symbols

α_{air}	air diffusivity (m^2/s)
α_c	curtain absorptivity
β_{air}	air thermal expansion coefficient (1/K)
ε	emissivity
θ	sun rays' average inclination towards the receiver (°)
λ	thermal conductivity (W/mK)
μ_{air}	air dynamic viscosity (Pa•s)
ρ_{air}	air density (kg/m^3)
ρ_p	particle density (kg/m^3)
ρ_c	curtain reflectivity
$\rho_{w,t}$	wall reflectivity, thermal
$\rho_{w,s}$	wall reflectivity, solar
$\rho_{w,w}$	wall reflectivity, weighted
σ	Stefan-Boltzmann constant (W/m^{2}K^4)
τ_c	curtain transmissivity
φ_p	particle volume fraction

Acronyms

1D	One-Dimensional
2D	Two-Dimensional
3D	Three-Dimensional
CFD	Computational Fluid Dynamics
CSP	Concentrating Solar Power
DNI	Direct Normal Irradiance
DO	Discrete Ordinates
FEM	Finite Element Method
FVM	Finite Volume Method
HTM	Heat Transfer Medium
MCRT	Monte Carlo Ray Tracing
PB	Power Block
PR	Particle Receiver
SNL	Sandia National Laboratories
ST	Solar Tower
TES	Thermal Energy Storage
1D	One-Dimensional

Subscripts

0	initial value
A	layer A
A-B	layer A to layer B
abs	absorbed
adv	advective
amb	ambient
B	layer B
B-C	layer B to layer C
c	curtain
C	layer C
C-out	layer C to outside
cav	cavity
conv	convective
c-w	curtain to wall
cav-A	cavity to layer A
f	property at film temperature
fc	forced convection
i	i-th element along falling coordinate
in	inlet
j	j-th element along width coordinate
k	k-th element along thickness coordinate
l	layer
nc	natural convection
out	outlet
p	particle
rec	receiver
w	wall
w-c	wall to curtain

Superscripts

*	fictitious
X	along width coordinate
Y	along falling coordinate
Z	along thickness coordinate

Carlo Ray Tracing (MCRT) method is used only to simulate sun rays coming from the heliostats to the boundary area around receiver where the MCRT method is coupled with Discrete Ordinates (DO) method which is used for assessing propagation and absorption of solar radiation inside the receiver itself. Thermal model inside the receiver included convective heat transfer between particles and air, absorption of solar radiation evaluated by means of the DO method, and thermal radiation between particles themselves and particles and surroundings that were also evaluated by means of DO method. Finally, solar radiation was separated from the thermal one by dividing the radiation spectrum in two bands: 0–4.5 μm and 4.5–1000 μm. Siegel et al. [8] developed a model to simulate coupled processes of gas flow, particle flow, solar irradiation, and heat transfer inside of the receiver. Similarly as in [7] DO method was adopted to simulate radiation heat transfer inside the cavity, however here DO method was not coupled with MCRT at the boundary of the system, instead concentrated solar radiation was

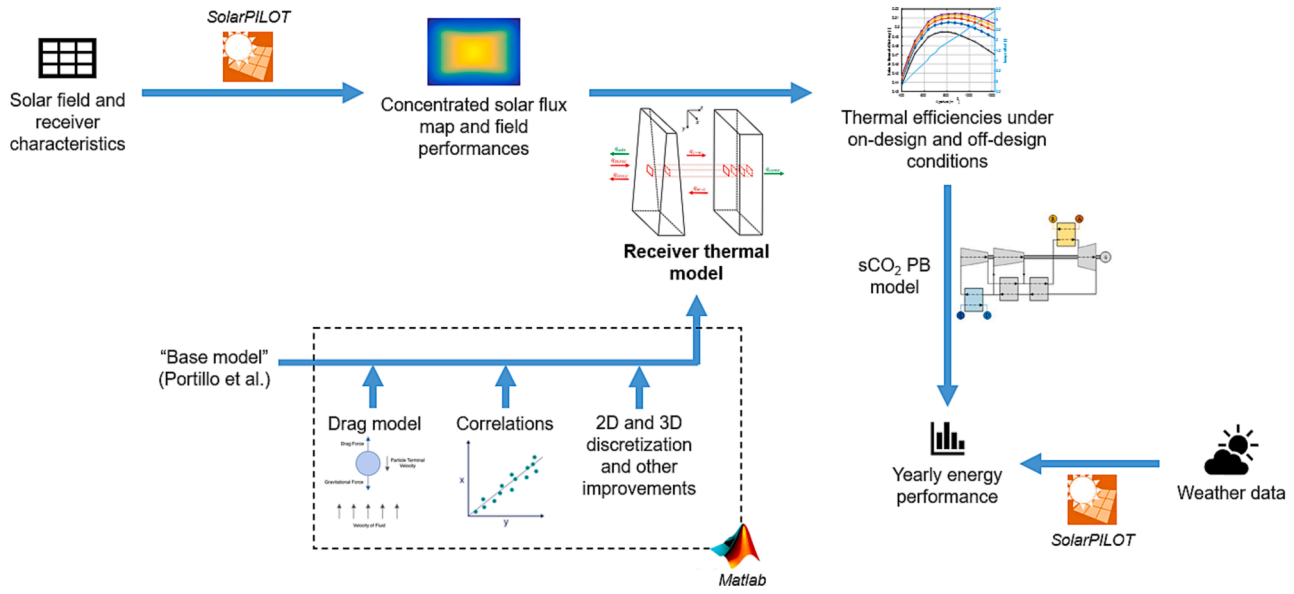

Fig. 1. Schematic diagram of the process followed for the receiver thermal model implementation and the system-level analysis of a particle-based solar tower plant.

simulated by means of a small "solar patch" that was applied at the middle of the aperture. They used FLUENT to solve the gas-phase mass, momentum, and energy balances, since cold air from the outside enters the receiver and circulates inside the hot cavity. Particle flow was also modelled by FLUENT by means of "time-integrated force balance on each particle that relates particle acceleration, drag, and gravitation Lagrangian reference frame". On the other hand, Wang et al. [9] adopted the Finite Element Method (FEM) together with MCRT to investigate transient heating of particles inside of the receiver. Distribution of solar radiation inside the receiver was simulated using MCRT while the heat transfer among the particles was calculated using FEM. To reduce the computational time, the model discretization was reduced from 3D to 2D (planar geometry). Other simplifying assumptions adopted in this work include adoption of uniform heat flux on the aperture, and the fact that external walls are considered adiabatic and heat loss occurs only through the aperture.

To the best of the authors' knowledge, only a few simplified thermal models suitable for system-level analyses are described in the literature. Röger et al. [10] developed a thermal model for a face-down cavity particle receiver. For the sake of simplicity, they considered only the radiation heat transfer, neglecting convective losses; the radiation-based model was obtained by adapting a code, which they previously used for radiation exchange in receivers closed with a semi-transparent fused silica window. González-Portillo et al. [11] implemented a simplified numerical model of the receiver for the techno-economic optimization of free-falling particle systems. The receiver model includes the curtain with a front part and a back part, a back wall, and it is 1D along the curtain height. It solves mass, momentum, and energy balances of the particle curtain, while for the back wall only energy balance is considered. This model was extended in [12] by fitting the advection coefficient correlation, wind effect, and view factor value against a more complex CFD model.

In this work, a falling particle receiver thermal model is implemented, starting from the model described in [11], henceforth referred to as the "base model". With respect to the base model, some important features are added to increase its level of detail and make it suitable for simulation of different types of falling particle receivers, regardless of their geometrical characteristics (see Section 2). Then, the developed thermal model is applied for the design optimization of different configurations of falling particle receivers and for the assessment of their yearly performance.

The work is organized as follows: Section 2 explains the methodology adopted to implement the receiver thermal model, as well as how to perform the whole plant yearly analysis; Section 3 presents the results of the model verifications; Section 4 describes the application of the developed methodology to a specific case study for the system-level analysis of a falling particle receiver; Section 5 shows the thermal model outcomes and the results of the aforementioned analysis; Section 6 draws the main work conclusions and anticipates possible future works.

2. Methodology

The methodology proposed to estimate the yearly performance of particle-based solar tower plants is described in Fig. 1. The conversion from solar energy to electricity is simulated through different models and tools: the solar field and receiver characteristics, as well as the weather data, are given as input to SolarPILOT v1.4.0 [13] that assesses the solar field performance and provides the heat flux maps on the receiver for each sun position and Direct Normal Irradiance (DNI) value; the thermal model developed in this work is then used for estimating the performance of particle receiver configurations under different conditions; finally, a sCO_2 PB model developed in previous work [14] is adopted to simulate the conversion of thermal to electric energy.

2.1. Receiver thermal model

The developed receiver thermal model is based on the stationary 1D model reported in [11] (i.e. the base model), which was verified against CFD simulations performed by Mills and Ho [15]. In the base model, some simplifications were adopted (e.g., uniform heat flux, constant particle specific heat, constant convective heat transfer coefficient), and some effects were not considered (e.g., drag force). Thus, the following features, which were not considered in the base model, are included in the model proposed in this work:

- Two-dimensional (2D) curtain discretization with non-uniform concentrated heat flux: particle curtain discretization is increased from 1D to 2D and thus a concentrated heat flux map can be used as solar input;
- Three-dimensional (3D) back wall discretization with 3D conduction: back wall discretization is increased from 1D to 3D thus implementing conduction heat transfer in all three directions to have the possibility of considering the adoption of multiple wall layers;

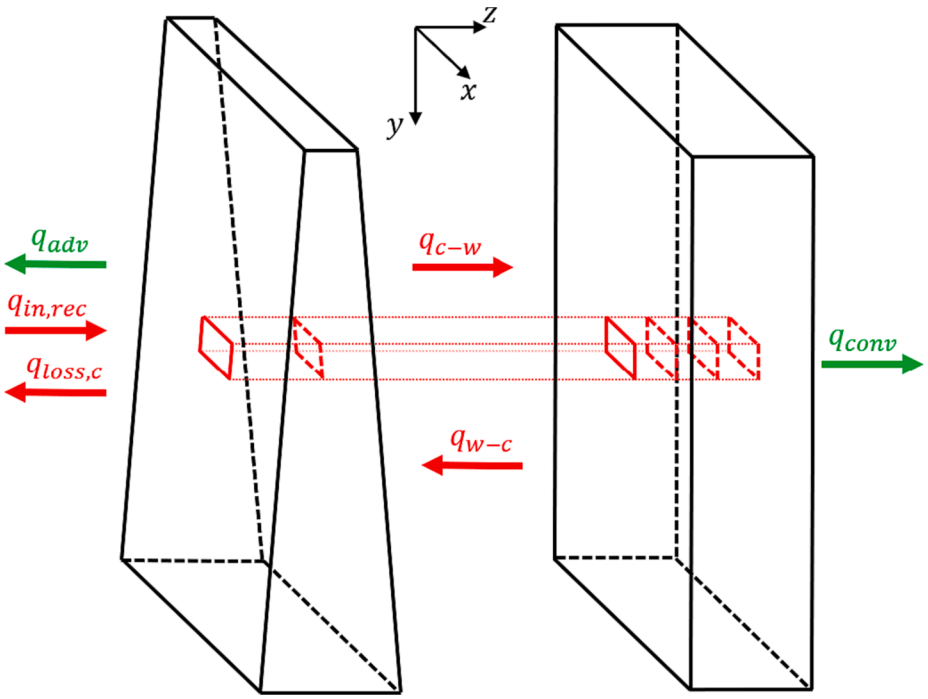

Fig. 2. Thermal model control volume discretization of the particle curtain (left-side element) and the back wall (right-side element), and heat transfer terms (red is for radiative while green is for others).

- Back wall insulation: an insulation layer is placed in the back wall stratigraphy, since in reality the adoption of an insulation layer is crucial, both for safety reasons and performance [16];
- Drag force effect: a drag model is implemented to consider the effect of drag in the particle curtain balances;
- Back wall variable reflectivity: back wall reflectivity changes with the wavelength (i.e., solar or thermal radiation);
- Convective heat transfer coefficient correlation: convective heat transfer as function of the wall temperature and air properties;
- Particle specific heat: particle specific heat depends as function of particle temperature;
- 3D-calculated equivalent view factor between particle curtain and aperture: an equivalent view factor allows to improve description of the interaction between particle curtain and cavity.

Both the particle curtain and the back wall are discretized into a certain number of control volumes along the falling direction (y) as well as along the width direction (x); moreover, the back wall is further discretized along the thickness direction (z), to estimate its temperature gradient.

A schematic visualization of the model discretization is provided in Fig. 2 where a single control volume of both curtain and the back wall is highlighted in red. The heat transfer terms as well as the curtain shape shown in Fig. 2 will be discussed in detail in the following sections.

More precisely, Section 2.1.1 describes the mass and momentum balances which enable assessment of the particle volume fraction and particle velocity, while Sections 2.1.2 and 2.1.3 show energy balances which are solved to assess the particle curtain and back wall temperatures. Please note that, for the sake of easier interpretation, in the following equations indices i and j, indicating i-th control volume along falling direction and j-th control volume along width direction, are not shown.

2.1.1. Mass and momentum balances

Mass flow rate per unit length $\dot{m}_p^{'}$ is calculated using Eq. (1), while mass balance (Eq. (2)) and momentum balance (Eq. (3)) equations for the particle curtain are solved in differential form to assess the value of particle volume fraction (φ_p) and particle velocity (v_p) in each control volume.

$$\dot{m}_p^{'} = \varphi_p t_c v_p \rho_p \tag{1}$$

$$\frac{d\dot{m}_p^{'}}{dy} = 0 \tag{2}$$

$$\frac{d\left(\dot{m}_p^{'} v_p\right)}{dy} = \varphi_p t_c \rho_p \left[g - a \frac{18}{d_p^2} \frac{\rho_{air}}{\rho_p} \frac{\mu_{air,f}}{\rho_{air,f}} \left(1 + b Re_f^{2/3}\right)\left(v_p - v_{air}\right) \right] \tag{3}$$

In Eqs. (1) and (3) t_c is the curtain thickness, ρ_p is the particle density, g is the gravitational acceleration, d_p is the particle diameter, v_{air} is the air velocity, ρ_{air} is the air density at ambient temperature, while $\mu_{air,f}$ and $\rho_{air,f}$ are dynamic viscosity and density of air at the local film temperature that is evaluated as the average of the particle temperature in the considered control volume and temperature of the ambient air.

As far as the air velocity (v_{air}) is concerned, according to [10], its value is assumed to be 60 % of the particle velocity in each control volume, since a similar average ratio was obtained through CFD simulations in [17]. Since the ratio of particle and air velocity, according to [10], depends on several boundary conditions, such as the exact cavity geometry, temperature distribution, and wind effects, the impact of this parameter is investigated in a sensitivity analysis presented in Appendix A.

The drag force effect in Eq. (3) is derived from a drag model presented by Hruby et al. [18], in which the Reynolds number is defined as:

$$Re_f = \frac{\rho_{air,f}\left(v_p - v_{air}\right) d_p}{\mu_{air,f}} \tag{4}$$

The drag model adopted does not consider the drag force acting on a single particle but mimics the drag effect on a particle curtain. A multiplier coefficient b for $Re_f^{2/3}$ of 0.15 was used in the model developed by Hruby et al. [18], however in this work a coefficient of 0.4 is chosen because that value is recommended in the same work [18] for

non-isothermal curtains with particles hotter than air, which is the case in this work.

The curtain thickness (t_c) is assumed to be a function of the falling distance (y): the starting value, $t_{c,0}$, (for $y = 0$) is evaluated by means of Eq. (5) [19], while its trend along the falling direction is assumed to be linear according to the experimental measurements performed by Kim et al. [20] , and it is defined in Eq. (6).

$$t_{c,0} = \left(\frac{60\dot{m}_p^{'}}{62\varphi_{p,0}\rho_p\sqrt{g}} \right)^{\frac{1}{1.5}} + 1.4d_p \tag{5}$$

$$t_c = t_{c,0} + 0.0087y \tag{6}$$

Several authors have suggested that the drag model might also include the particle volume fraction as a variable, as it could improve the matching of the model outcomes with the ones of a real particle curtain [21–23]. However, as discussed in Appendix B, correction factor effect is eliminated by setting a equal to one, because it provides worst matching for the most representative case of experimental velocity results and since its effect on the thermal model outcomes is negligible.

2.1.2. Particle curtain energy balance

Energy balance for the curtain is required to assess the value of temperature in each control volume; temperature is assumed to be uniform along the thickness of the curtain (z direction) in Fig. 2.

The energy balance of the curtain (Eq. (7)) is derived by considering all the power that is entering and exiting a control volume using a discrete approach.

$$-q_{abs,c} + q_{in,rec} - q_{loss,c} - q_{c-w} + q_{w-c} - q_{adv} = 0 \tag{7}$$

where:

- $q_{abs,c}$ is the thermal power absorbed by the curtain in the control volume, computed employing the Eq. (8).

$$q_{abs,c} = \frac{\dot{m}_p^{'}\left(c_{p,out}T_{p,out} - c_{p,in}T_{p,in}\right)}{\Delta y} \tag{8}$$

  where T_p is the particle temperature, c_p is the particle specific heat and Δy is the control volume length in the falling direction. Particle specific heat is evaluated trough the temperature dependent correlation which is reported in Section 4. Please note that "in" and "out" indicate variables' values at the inlet and outlet of the control volume respectively.
- $q_{in,rec}$ is the solar input in the control volume obtained as output from SolarPILOT;
- $q_{loss,c}$ is the radiative loss from the front part of the curtain, evaluated by means of Eq. (9). It considers the emitted radiation from the curtain, the solar input being reflected, and the incoming radiation from the back wall being transmitted. Please note that the effect of the radiation from the ambient is not considered as it was also not considered in the base model, however it is evaluated that in the design conditions of the optimal configuration of the free-falling particle receiver, determined in Section 5.1, radiation loss is only 0.8 % lower when the effect of the ambient radiation is included.

$$q_{loss,c} = F_{eq}\left(\varepsilon_c\sigma T_p^4 + \rho_c q_{in,rec} + \tau_c q_{w-c}\right) \tag{9}$$

  where ε_c is the curtain emissivity, σ is the Stefan-Boltzmann constant, ρ_c is the curtain reflectivity and τ_c is the curtain transmissivity. F_{eq} is the equivalent view factor evaluated using the Eq. (10).

$$F_{eq} = F + (1-F)\left(1 - \rho_{w,t}\alpha_{c,average}\right) \tag{10}$$

  F_{eq} is obtained by taking into consideration the geometrical view factor (F) between the current control volume and the aperture which indicates radiative power which is lost directly to the ambient. Remaining part of Eq. (10) indicates radiative power that is coming from the control volume towards internal walls of the cavity and is lost to the ambient. As a conservative assumption, this fraction of radiative power is assumed to be equal to all radiative power coming to the internal cavity walls except power that is reflected by the walls and then absorbed by the particle curtain, being $\rho_{w,t}$ and α_c the back wall thermal reflectivity and the curtain absorptivity, respectively. 3D view factors (F) are calculated using the MATLAB® function "viewfactor" [24];
- q_{c-w} is the radiative power going from the curtain towards the back wall, evaluated using Eq. (11).

$$q_{c-w} = \varepsilon_c\sigma T_p^4 + \tau_c q_{in,rec} + \rho_c q_{w-c} \tag{11}$$

- q_{w-c} is the radiative power going from the back wall towards the curtain, evaluated using Eq. (12).

$$q_{w-c} = \varepsilon_w\sigma T_{i,j,cav-A}^4 + \rho_{w,t}\varepsilon_c\sigma T_p^4 + \rho_{w,s}\tau_c q_{in,rec} + \rho_{w,w}\rho_c q_{w-c} \tag{12}$$

where ε_w is the back wall emissivity, $T_{i,j,cav-A}$ is the surface temperature of the internal part of the back wall in the control volume (i,j), $\rho_{w,s}$ is the back wall solar reflectivity, and $\rho_{w,w}$ is the back wall weighted reflectivity (calculated as reported in Appendix C). Indeed, the model is implemented to consider different values of reflectivity for the internal side of the back wall depending on the source of the radiation. For the solar radiation, reflectivity value corresponding to $\rho_{w,s}$ is used, while the radiation that originates from the particle curtain or the back wall is reflected with the reflectivity value corresponding to $\rho_{w,t}$. This is done since in real receivers back wall properties are selected both to minimize the thermal losses and to reduce the solar radiation absorption [16]. Please note that directional dependence of the radiation is not included in the model, as in the base model developed by González-Portillo et al. [11], meaning that emissions from control volume (i,j) of the curtain only interact with the control volume (i,j) of the back wall, and vice-versa.

- q_{adv} is the advective loss from the front part of the curtain assessed using Eq. (13).

$$q_{adv} = h_{adv}\left(T_p - T_{amb}\right) \tag{13}$$

  where T_{amb} is the ambient temperature and h_{adv} is the advective heat transfer coefficient. Calculation of h_{adv} is done by means of the correlation reported in [11] obtained by fitting the CFD results from Mills and Ho [15] (Eq. (14)). However, it should be noted that even though wind can have large impact on the thermal efficiency of the receiver, and in particular on the advective losses, impact of wind is not taken into the account in this corelation, as Mills and Ho [15] neglected this effect in their simulations, and therefore it is also not considered in the current work.

$$Nu_{adv} = \frac{h_{adv} \bullet h_{curtain}}{k_{air}} = -758.9 + 0.05737 \bullet \left(Re^*\right)^{\frac{6}{7}} \tag{14}$$

This correlation provides a single value of Nusselt number (Nu_{adv}) to be used for the whole curtain. Nu_{adv} is computed as function of a Reynolds number that is obtained considering the particles' velocity at the bottom of the curtain and the air thermophysical properties at the average temperature between the curtain average temperature and the air temperature. Due to the significant uncertainty regarding the advective heat transfer coefficient, its impact on the receiver thermal efficiency is investigated with a dedicated sensitivity analysis (see Appendix A). Since the CFD simulation performed by [15]

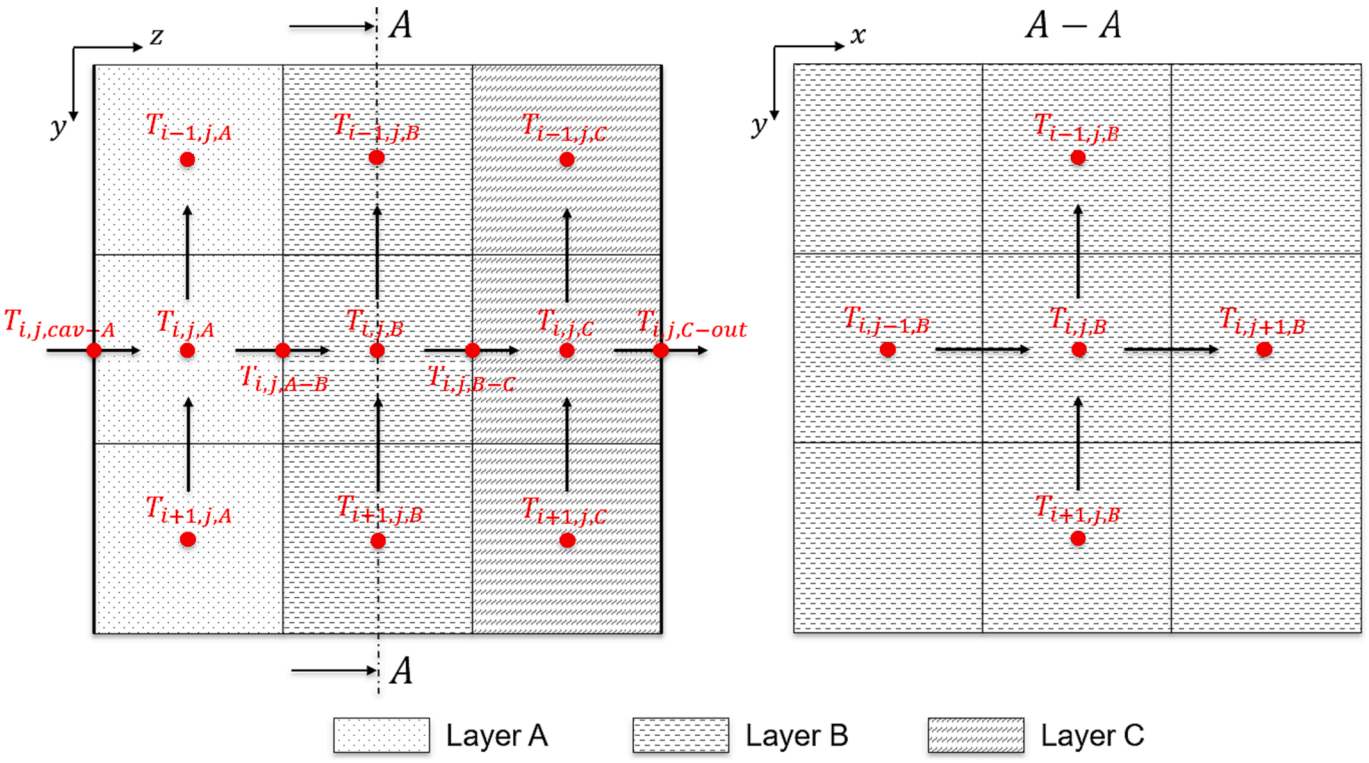

Fig. 3. Back wall temperature discretization (x is the width coordinate, y is the falling coordinate and z is the thickness coordinate). Black arrows indicate the direction adopted as positive for heat transfer in the back wall. Square shape for control volumes is adopted just for the sake of simplicity and it is not strictly the actual one.

takes into account the drag effect while the model in [11] does not, the Reynolds number (Re^*) is evaluated as function of a fictitious particles' velocity (v_p^*) obtained through Eq. (15).

$$v_p^* = \sqrt{v_0^2 + 2gh_{curtain}} \tag{15}$$

where v_0 is the initial particle velocity which is evaluated with Eq. (16).

$$v_0 = \frac{\dot{m}_p'}{t_{c,0}} \tag{16}$$

2.1.3. Back wall energy balances

For what concerns the back wall, it is assumed to be subdivided into three layers (namely "A", "B" and "C") in the thickness direction (z), in which both volume temperatures (in the middle of each layer) and nodal temperatures (at the interfaces between layers or at the interface between layer and cavity/ambient) are evaluated.

Fig. 3 provides a schematic overview of the back wall 3D discretization showing the different wall temperatures assessed in the thermal model as well as the heat fluxes. Please note that, in this section, indices of control volumes will be represented as there is the heat exchange between them.

The first balance (Eq. (17)) is useful to assess the surface temperature ($T_{i,j,cav-A}$) of the part of the back wall which is seeing the cavity; it is derived by following the same approach adopted in Eq. (7) and considering conduction between $T_{i,j,cav-A}$ and the first layer volume temperature ($T_{i,j,A}$), being λ_A the inner layer thermal conductivity and t_A the inner layer thickness.

$$-\frac{2\lambda_A}{t_A}\left(T_{i,j,cav-A} - T_{i,j,A}\right) + q_{c-w} - q_{w-c} = 0 \tag{17}$$

For the assessment of the temperatures inside the wall ($T_{i,j,A}$, $T_{i,j,A-B}$, $T_{i,j,B}$, $T_{i,j,B-C}$, $T_{i,j,C}$), five balances, following the equation structure presented in Eq. (18), are required.

$$\dot{Q}_{cond}^{Z} + \dot{Q}_{cond}^{Y} + \dot{Q}_{cond}^{X} = 0 \tag{18}$$

where:

- $\dot{Q}_{cond}^{Z}$ is the conduction power along the thickness coordinate (z). It is the only term always present in the balances and it is calculated using Eq. (19).

$$\dot{Q}_{cond}^{Z} = \Delta y \Delta x \frac{2\lambda_l}{t_l}\left(T_{i,j,k-1} - T_{i,j,k}\right) - \Delta y \Delta x \frac{2\lambda_l}{t_l}\left(T_{i,j,k} - T_{i,j,k+1}\right) \tag{19}$$

where Δx is the control volume width, λ_l and t_l are the thermal conductivity and the thickness of the layer in which the balance is performed, respectively, and k is the index that moves along the thickness direction taking the values shown in Eq. (20).

$$k = \{cav\text{-}A; A; A\text{-}B; B; B\text{-}C; C; C\text{-}out\} \tag{20}$$

- $\dot{Q}_{cond}^{Y}$ is the conduction power along the falling coordinate (y). It is not present in the balances for the interfaces between the layers, as it can be seen in Eq. (21).

$$\dot{Q}_{cond}^{Y} = t_l \Delta x \lambda_l \frac{\left(T_{i+1,j,k} - T_{i,j,k}\right)}{\Delta y} - t_l \Delta x \lambda_l \frac{\left(T_{i,j,k} - T_{i-1,j,k}\right)}{\Delta y} \quad \text{if} k = \{A; B; C\} \tag{21}$$

- $\dot{Q}_{cond}^{X}$ is the conduction power along the width coordinate (x). As well as $\dot{Q}_{cond}^{Y}$, it is not present at the interfaces between the layers, and it is calculated with Eq. (22).

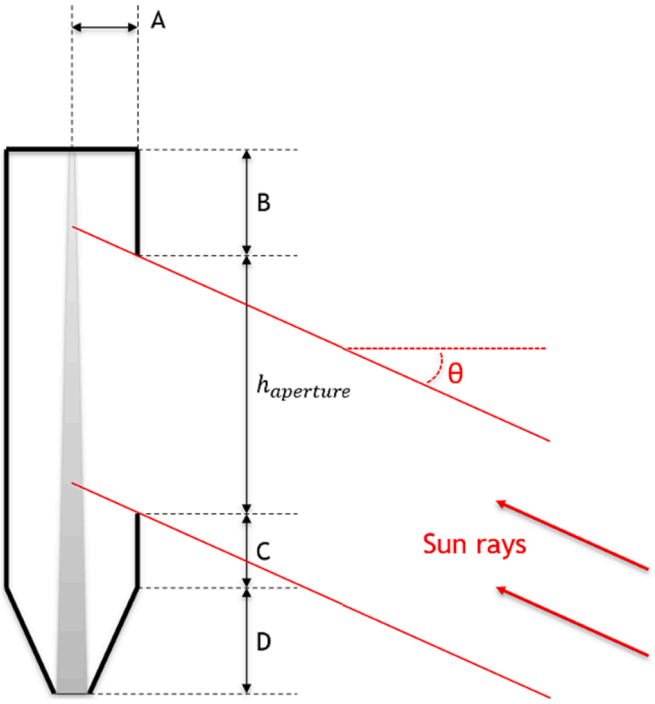

Fig. 4. Cavity geometry implemented in this work.

$$\dot{Q}^{X}_{cond} = t_l \Delta y \lambda_l \frac{(T_{i,j-1,k} - T_{i,j,k})}{\Delta x} - t_l \Delta y \lambda_l \frac{(T_{i,j,k} - T_{i,j+1,k})}{\Delta x} \quad \text{if} k = \{A; B; C\} \tag{22}$$

The last balance to be solved is performed at the surface of outer part of the back wall. Since the outer layer is in contact with the ambient, convection heat transfer is considered, leading to Eq. (23). Please note that radiation heat transfer towards the ambient is not considered as it was also not considered in the base model (this assumption is validated by the fact that outer surface of the back wall for the regular curtain does not exceed 70 °C).

$$\frac{2\lambda_C}{t_C}\left(T_{i,j,C} - T_{i,j,C-out}\right) - q_{conv} = 0 \tag{23}$$

where q_{conv} is the convective heat flux, calculated by means of Eq. (24).

$$q_{conv} = h_{conv}\left(T_{i,j,C-out} - T_{amb}\right) \tag{24}$$

The convective heat transfer coefficient (h_{conv}) is derived by following the approach applied in [25] for flat plate reported in Eq. (25).

$$h_{conv} = h_{conv,nc} + h_{conv,fc} \tag{25}$$

where $h_{conv,nc}$ is the convective heat transfer coefficient estimated as if only pure natural convection is occurring while $h_{conv,fc}$ is the one that considers forced convection only.

The natural convection heat transfer coefficient ($h_{conv,nc}$) is evaluated through a local correlation (Eq. (26)) for vertical plate, reported in [25,26]. This correlation permits to assess $h_{conv,nc}$ as function of the distance ($\tilde{y}$) between the centre of the current control volume and the bottom of the back wall. The value of $h_{conv,nc}$ depends both on the convective heat loss ($\dot{Q}_{conv}$) in the control volume and on coefficients C and n which depend on the flow regime (Eqs. (27) and (28)), while the air thermophysical properties are evaluated at the local film temperature.

$$h_{conv,nc} = \lambda_{air,f} C^{\frac{n}{n+1}} \left(\frac{g\beta_{air,f}\rho_{air,f}}{\lambda_{air,f}\mu_{air,f}\alpha_{air,f}}\right)^{\frac{1}{n+1}} \left(\frac{\dot{Q}_{conv}}{\Delta y \Delta x}\right)^{\frac{1}{n+1}} \tilde{y}^{\frac{3-n}{n+1}} \tag{26}$$

$$C = \begin{cases} \dfrac{\left(\dfrac{0.75 Pr^{0.5}}{\left(0.609 + 1.221 Pr^{0.5} + 1.238 Pr\right)^{\frac{1}{4}}}\right)^{\frac{5}{4}}}{Pr^{\frac{1}{4}}} & \text{if} Ra_{\tilde{y}} < 10^9 \\ 0.13 & \text{if} \quad Ra_{\tilde{y}} > 10^9 \end{cases} \tag{27}$$

$$n = \begin{cases} 4 \text{ if} & Ra_{\tilde{y}} < 10^9 \\ 3 & \text{elsewhere} \end{cases} \tag{28}$$

The forced convection heat transfer coefficient ($h_{conv,fc}$) is evaluated through a global correlation (Eq. (29)) for a flat plate, reported in [25]. The velocity considered for the computation of Re_{fc} is the wind velocity and the air thermophysical properties are evaluated at the average temperature between the back wall temperature and the air temperature. The average wind velocity on the top of the tower at the location of the plant is taken from Global Wind Atlas 3.0 using the Hellman law shown in Eq. (30) where z_0 indicates height at which wind speed is measured, and α is the coefficient which is typically taken equal to 1/7.

$$h_{conv,fc} = 0.0287 Re_{fc}^{0.8} Pr^{1/3} \tag{29}$$

$$v_{wind}\left(h_{optical,tower}\right) = v_{wind}(z_0)\left(\frac{h_{optical,tower}}{z_0}\right)^{\alpha} \tag{30}$$

2.1.4. Particle curtain optical properties model

Since most of the power exchanged in the system is in radiative form (>90 %), an accurate assessment of the values of curtain optical properties as function of the curtain physical and geometrical characteristics is extremely important. A model developed by González-Portillo et al. [27], and verified against a MCRT model, is used to assess the value of absorptivity, transmissivity and reflectivity of the particle curtain.

The model adopts a probabilistic approach to evaluate the optical properties and provides a set of equations used for their assessment, giving the possibility of evaluating their values as function of particle absorptivity, particle diameter, particle volume fraction, and curtain thickness. Further details about the model can be found in [28].

The sensitivity of the model to the particle volume fraction and curtain thickness allows for the values of the optical properties to change according to the receiver operating conditions, while the sensitivity to the particle absorptivity and particle diameter permits to study the impact of changing the type of particles on the receiver performance.

2.1.5. Receiver cavity

Although the developed model could work with almost any shape of the cavity with certain modifications, in this study, the geometry reported in [29] is considered as a starting point; in particular, Fig. 4 shows all the dimensions required by the model.

Moreover, the model automatically assesses the geometrical view factor of three different curtain areas: the irradiated one, the one above, and the one below. Each control volume adopts the geometrical view factor of its specific area to assess its equivalent view factor.

To assess the aforementioned geometrical parameters, Eqs. (31)–(36) are derived by adopting an approach devised by the authors and using proportions from [29] stated in Eqs. (35) and (36), that would respect the physics of the system as well as protect the upper part of the receiver from being exposed to sun rays. Final thickness ($t_{c,final}$) that the curtain would have for a specific curtain height ($h_{curtain}$) is the starting point for the sizing. The average inclination (θ) of the sun rays reflected by the heliostats is computed as function of the aperture height ($h_{aperture}$), with a correlation that depends on the specific solar field and optical height of the tower, and thus it is case dependent. More details on how θ can be estimated are provided in Section 2.2.1.

$$t_{c,final} = t_{c,0} + 0.0087 h_{curtain} \tag{31}$$

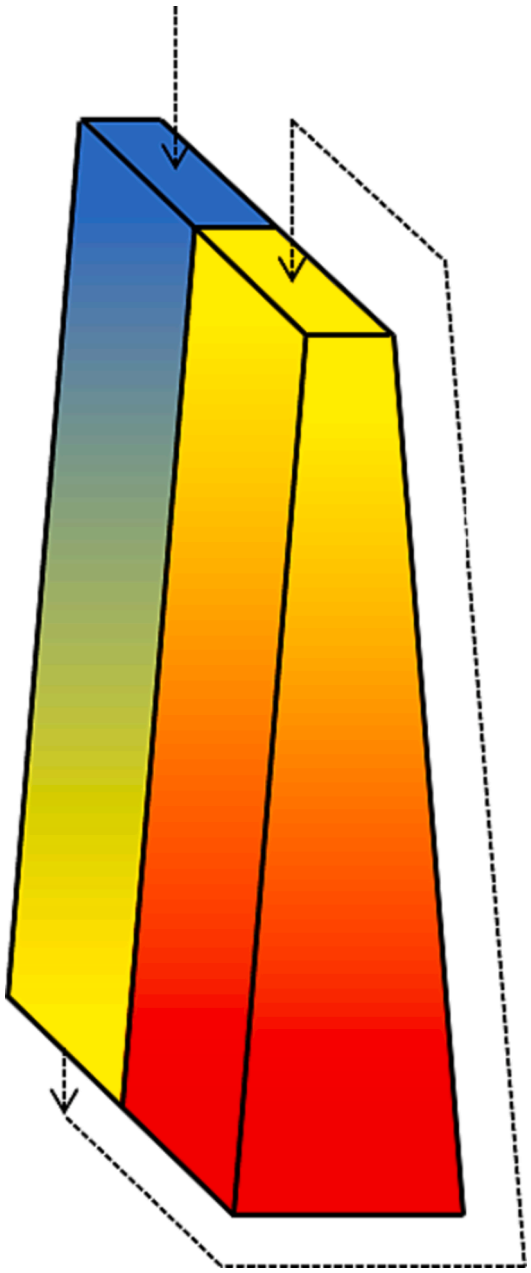

Fig. 5. Working principle of recirculation. Colour gradient represents the expected temperature increase along the particle fall (blue and red are the coldest and hottest curtain parts, respectively).

$$\theta = f\left(h_{aperture}\right) \tag{32}$$

$$A = 2.5t_{c,final} \tag{33}$$

$$B = 0.5 + 2Atan\theta \tag{34}$$

$$D = B \tag{35}$$

$$C = \frac{1.4}{2}D \tag{36}$$

2.1.6. Multistage

A way to increase the performance of the free-falling particle receivers is the adoption of the so called multistage configuration [30]. It consists of adopting troughs that collect particles and which aim is to reduce the particle velocity and increase the particle volume fraction, thus reducing advection losses and increasing opacity of the curtain.

The model described in this work can be used also to evaluate the multistage configuration performance in a simplified way. In detail, it is considered that trough restarts the curtain with same initial velocity and thickness. As a first approximation, it is assumed that particles leave the trough at uniform temperature (i.e., ideal mixing). The validity of this assumption will be investigated in Section 5.1 by comparing thermal efficiency of ideal mixing to the thermal efficiency of the case with no mixing inside the troughs.

2.2. Yearly performance assessment

As described in Fig. 1, the developed thermal model can be employed for performing the system-level analysis of a particle-based solar tower plant. Methodology adopted for the assessment of the yearly performance is shown in this section. It should be noted that the scope of this work is the evaluation of the particle receiver performance and therefore, the economic analysis is out of scope of this work, and it will be analysed in future works.

2.2.1. Optical analysis

Once the solar field and receiver characteristics (e.g., tower optical height, heliostat dimensions, receiver dimensions, etc.) are provided as input, SolarPILOT [13] is used for performing the optical analysis of the solar plant. Optical analysis for on-design sizing of the receiver consists of simulating the solar field under design conditions with the purpose of obtaining the heat flux map on the particle curtain and the field performance for multiple aperture sizes. Yearly optical performance analysis consists in evaluating optical efficiency of the solar field, using SolarPILOT, for each hour of the year which is then, along with weather data, given as input to the yearly simulation to determine the incident energy on the receiver.

An additional analysis carried out in SolarPILOT [13] is the calculation of the sun rays' average inclination (θ), weighted on energy, as function of the receiver aperture. This angle is used for sizing the receiver cavity as described in Section 2.1.5, idea is that using the average angle of sun rays it is possible to calculate the necessary height of the wall above the receiver aperture to properly position aperture of the receiver with respect to the concentrated heat flux hitting the particle curtain. To do so, solar field is simulated by varying the receiver size and inclination in the settings of SolarPILOT, and collecting the values of inclination angles which lead to the highest optical efficiency that is representative of the condition of orthogonality between sun rays and receiver aperture. With those results, an equation can be derived by curve fitting. Since the results are affected by both the solar field and the tower optical height, the obtained correlation is case dependent.

2.2.2. On-design optimization

The model described in Section 2.1 is used to assess the thermal efficiency while varying the receiver aperture to determine the optimum aperture size of each configuration. The aiming strategy adopted to derive the heat flux map is image size priority [13]. Heat flux maps are obtained by targeting aim points on a flat receiver which is considered to be positioned where the particle curtain is. To maximize the optical efficiency at each given aperture size, the image offset is varied to reach the maximum admittable peak flux.

2.2.3. Off-design performance assessment

The particle receiver is simulated varying the DNI from a maximum value to the minimum one that permits the receiver to operate under the desired conditions. Thus, obtaining the off-design performance curve of the receiver.

The adoption of a strategy meant to increase the receiver performance is investigated. Indeed, Röger et al. [10] proposed a way to improve the off-design performance and extend the receiver operating range: the so called recirculation. Working principle is shown in Fig. 5;

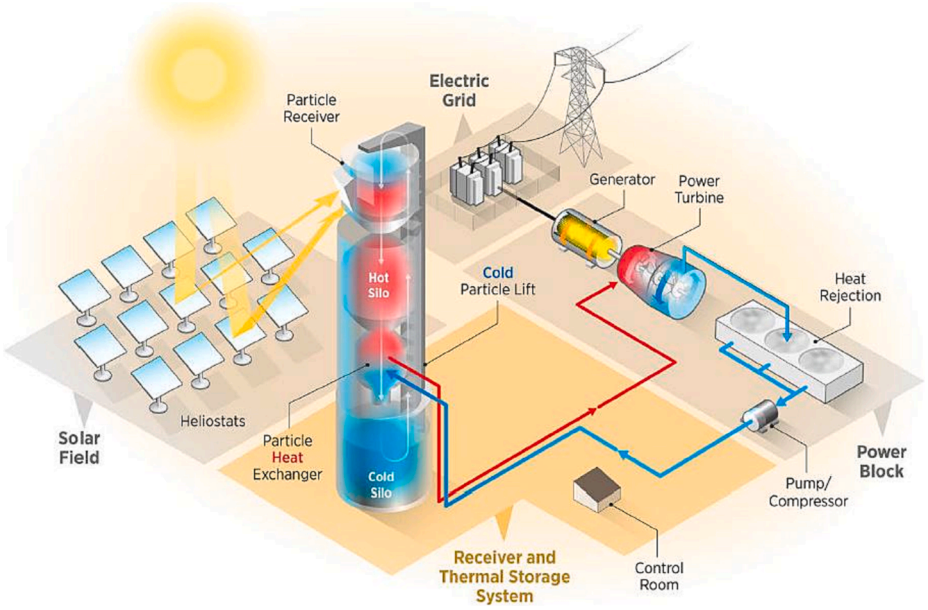

Fig. 6. Plant schematic [3].

the particle curtain is divided in two smaller curtains in the width direction: particles firstly fall on one side, then are recirculated back on the other side by means of an additional elevator, falling again on that side. This is done to increase the mass flow rate per unit length, and thus to increase the opacity of the curtain at low incident solar power. However, disadvantages of the recirculation are adoption of an additional elevator, and additional complexity.

2.2.4. Yearly analysis

The off-design curves obtained following the methodology explained in the section above are used to calculate the thermal efficiency as function of the solar thermal input (coming from optical analysis, see Section 2.2.1) for each hour during the year.

To perform the yearly analysis, a sCO_2 PB model [14] is used in combination with TES. Heat exchange between the particles and sCO_2 working fluid takes place inside the Primary Heat Exchanger which, according to the operating conditions stated in [3], has 50 °C temperature difference on the hot side and 25 °C difference on the cold side. For simplicity thermal efficiency of the Primary Heat Exchanger is assumed equal to 100 %. Integration of TES and PB with the solar tower and the solar field can be visualized in Fig. 6.

The strategy adopted to operate the plant is to always run the PB at its nominal thermal power input. If the thermal energy coming from the receiver is not enough to do so, the TES is going to be discharged if possible, otherwise, if it does not have enough thermal energy stored, the PB will be shut down and the TES will be filled with all the incoming thermal energy.

The electric power needed for the elevator is computed by means of Eq. (37) [11], where h_{lift} is the elevator height (computed for both main elevator and optional recirculation one). The main elevator height is function of the optical height of the tower ($h_{optical,tower}$), of the heliostat height ($h_{heliostat}$), of the aperture height ($h_{aperture}$), as well as of cavity dimensions (B).

$$P_{lift} = \frac{\dot{m}_p' w_c h_{lift} g}{\eta_{lift}} \tag{37}$$

$$h_{lift} = \begin{cases} h_{optical,tower} + \frac{h_{heliostat}}{2} + \frac{h_{aperture}}{2} + B - A tan\theta & \text{for main elevator} \\ h_{curtain} & \text{for recirculation elevator} \end{cases} \tag{38}$$

When considering the adoption of recirculation, its convenience with respect to the regular curtain is evaluated hour-by-hour by considering both the thermal efficiency values at given input solar power and the additional elevator consumption. Then, recirculation is adopted if it appears to have better performance than the regular curtain at that specific condition.

3. Receiver model verification

Firstly, it is evaluated if the base model developed in [11] is implemented correctly. Two solar inputs reported are considered, namely 750 MW_{th} and 375 MW_{th}, and the resulting mean absolute errors for the total losses in those cases are 0.2 % and 0.6 %, respectively. As good matching with the original model is obtained, it is possible to proceed with the following verifications:

- Verification of the drag model against model and experimental results reported by Hruby et al. [18];
- Verification of the developed thermal model against CFD simulation reported by Mills et al. [29].

3.1. Drag model verification

This verification is necessary considering that the starting model presented in [11] does not consider the effect of drag forces. The drag model implemented in this work is used to simulate three different particle curtain conditions, and its outcomes are compared to the outcomes of both the model developed by Hruby et al. [18] and the results of their experimental measurements.

Before showing the comparison results it is worthy to stress the differences between the model adopted in this work and the one in [18]. Firstly, in [18] the velocity of entrained air is calculated by means of gas phase equations while the model presented in this work considers that the velocity of entrained air is equal to 0.6 times the velocity of the particles, as it was described in Section 2.1.1. Secondly, as mentioned earlier, a factor b of 0.4 is assumed, as it is recommended in [18] for non-isothermal curtains with particles hotter than air, instead of 0.15 which they initially used in their model for obtaining the curves shown in Fig. 7.

Fig. 7a, b and c present results at elevated particle temperatures and

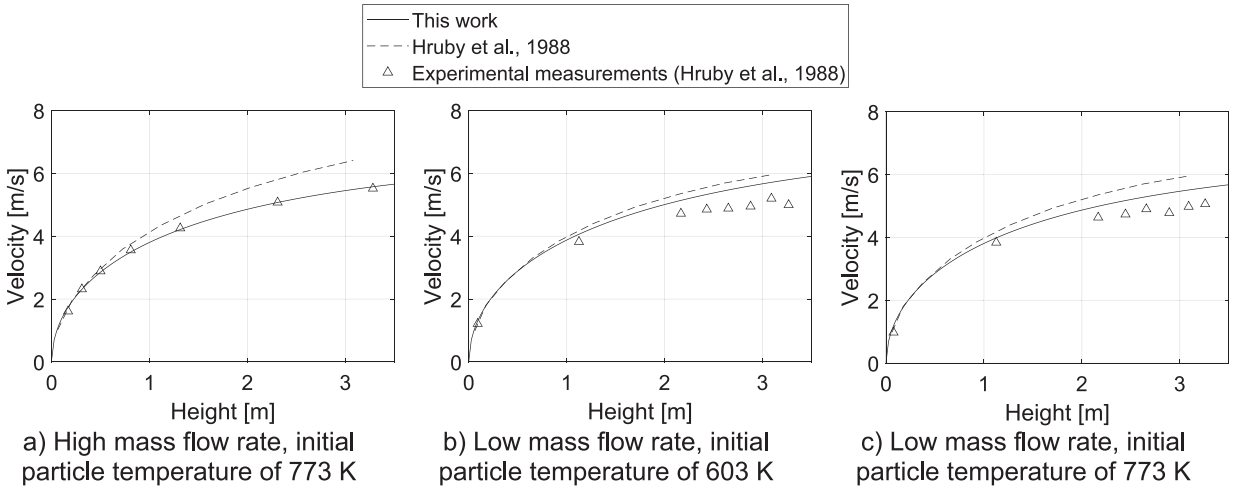

Fig. 7. Drag model verification results.

different flow rates. "Low mass flow rate" in the figures indicates mass flow rate per unit length of 0.31 kg/s/m while "high mass flow rate" indicates mass flow rate per unit length of 0.78 kg/s/m. It can be seen in Fig. 7b and c that velocity is overestimated compared to the experimental results, but that overestimation is lower compared to the one of the model presented by Hruby et al. [18]. Meanwhile, in the case of high mass flow rate and inlet temperature of 773 K (Fig. 7a) the model almost perfectly approximates experimental measurements. However, it should be added that considered mass flow rates in this verification procedure are relatively low compared to the values targeted for commercial applications (10–20 kg/s/m according to [3]) and therefore presented drag model should be additionally verified at higher values of mass flow rate.

3.2. Thermal model verification

In this section, the results provided by the developed thermal model are compared to those of the CFD simulation described in Mills et al. [29], which is a work introducing significant approximations on the fluid-particle interactions and the radiative heat transfer model and therefore should only serve as guidance. More precisely, three versions of the developed thermal model are considered:

- "Base case": without any improvement, essentially the model presented in [11], but with different geometry;
- "Drag": all improvements;
- "No drag": all improvements except drag force effect.

Main receiver characteristics and operating conditions are reported in Table 1. As only overall value of incident power on the receiver is provided, flux is assumed to be uniform over the aperture area.

Table 1
Thermal model verification receiver characteristics.

Parameter	Value
Incident power on the receiver	2.55 MW_{th}
Particle inlet temperature	575 °C
Particle outlet temperature	775 °C

Table 2
Results of the model verification against CFD simulation provided in [29].

	CFD	Base case	Drag	No drag
Efficiency (%)	86.9	87.9	87.7	85.8
Radiative losses (%)	9.1	7.6	8.4	10.3
Advective losses (%)	3.4	3.4	3.5	3.5
Convective losses (%)	0.6	1.2	0.5	0.5

The values of thermal efficiency and thermal losses for CFD and for the three considered cases are reported in Table 2.

Table 2 shows that the case "Drag" provides the best matching with CFD results. Besides matching the efficiency, "Drag" case also provides better matching of both radiative (include both radiative and optical losses) and convective losses (energy transferred from the back wall to the ambient by means of convection), while advective losses (energy transferred from the particle curtain to the air inside the receiver cavity) error is relatively small even though it is larger than one of the "Base case". It is worth mentioning that the only difference between "Drag" and "No drag" results is in the radiative losses, this is because the absence of drag force in "No drag" implies higher velocity thus resulting in lower absorptivity of the particle curtain.

Results of this verification justify the adoption of the "Drag" case in the further analysis performed in this work, which will be described in the following sections. In addition, based on the results of this verification, the thermal model developed in this work can be deemed suitable for system-level analysis of falling particle receivers as it provides results in line with those obtained through CFD simulation with a limited computational cost. In detail, the simulation of current operating condition requires around 4 min on OMEN by HP Laptop 15 with a 16 GB RAM and Intel Core i7-9750H CPU 2.60 GHz processor.

4. Case study

The developed receiver thermal model is applied for a specific case study to perform the on-design sizing of different configurations of the particle receivers for a given solar field. Subsequently, for the obtained configurations, off-design and yearly performance are evaluated.

Investigated configurations, shown in Fig. 8, are the regular curtain and multistage configurations ranging from two to five stages. For the sake of simplicity, it is assumed that troughs are uniformly arranged in the irradiated part of the curtain, as it can be observed in Fig. 8.

Daggett, California (34.86609, −116.88806) is selected as location, and the weather file is retrieved from SolarPILOT [13]. Solar field, with a solar multiple equal to 2.4, is generated considering the design DNI of 1000 W/m^2 and the sun position corresponding to the summer solstice at solar noon in SolarPILOT [13], based on the characteristics of the 100 MW_{el} plant described in [3]. According to the same reference, the thermal input to the heat transfer medium after losses is 550 MW_{th}, size of the aperture is around 30 m, thermal losses are 60 kW/m^2 based on the aperture area, and average absorptivity is 94 %. Based on this information, it is possible to determine the incident power on the receiver that solar field should provide, and to generate the field in SolarPILOT.

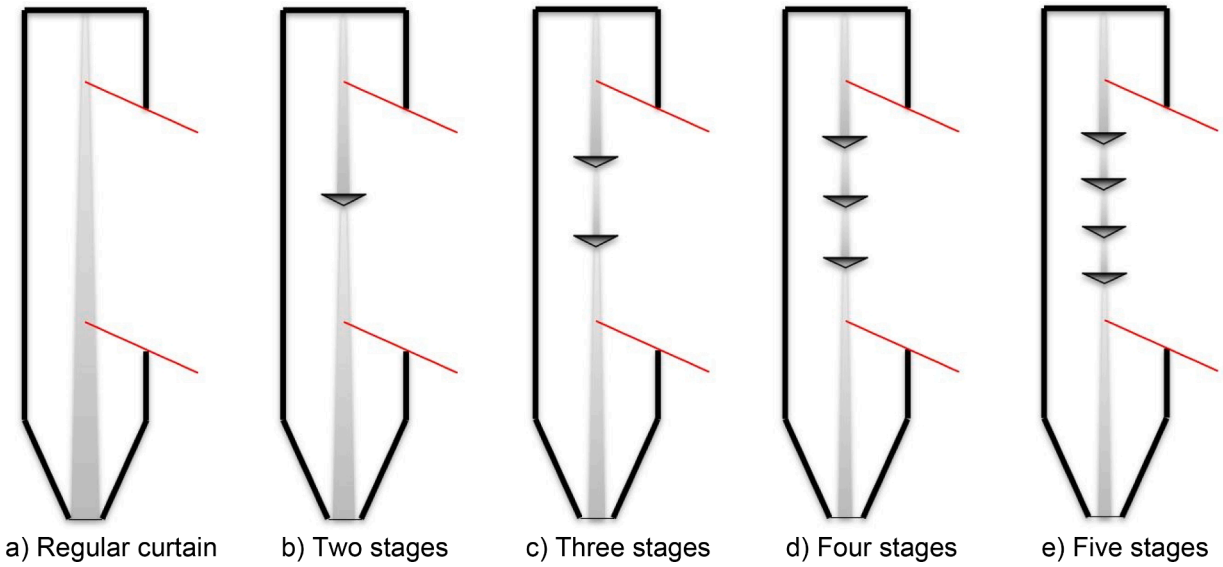

Fig. 8. Falling particle receiver configurations considered in this work.

Table 3
Assumptions adopted in the case study.

Parameter	Value	References
Solar field		
Tower optical height	270 m	[3]
Heliostat area	144 m^2 (12 × 12 m)	[3]
Heliostat surface slope error	1.53 mrad	[3]
Heliostat reflectivity	0.95	[34]
Number of heliostats	8225	
Receiver		
Particle inlet temperature T_{in}	575 °C	[3]
Particle outlet temperature T_{out}	750 °C	[3]
Back wall emissivity ε_w	0.8	[11]
Particle diameter d_p	350•10^{-6} m	[11]
Particle density ρ_p	3550 kg/m^3	[11]
Initial volume fraction $\varphi_{p,0}$	0.6	[11]
Particle absorptivity α_p	0.87	[11]
Particle emissivity ε_p	0.87	[11]

Assumptions on the heliostats and receiver characteristics are reported in Table 3, while the field itself with its optical efficiency, which does not consider intercept factor, is shown in Fig. 9.

The particle specific heat depends on the particle temperature according to the correlation adopted by [15] and developed by means of data fitting by SNL [19]. In the correlation (Eq. (39)) the particle temperature is in Celsius degrees (°C), and it is valid for the particle type CARBO ACCUCAST ID50 in the temperature range: $50\,^{\circ}C \leq T_p \leq 1000\,^{\circ}C$.

$$c_p = 365 \bullet T_p^{0.18} \tag{39}$$

Correlation for the average inclination (θ) of the sun rays reflected by the heliostats of this plant is reported in Eq. (40).

$$\theta = 32.77 + 0.22 h_{aperture} \tag{40}$$

Back wall consists of three layers of thickness equal to 25.4 mm whose composition is taken from [16]. Inner layer, which sees the particles, is made of the RSLE-57 board, with thermal conductivity taken from [31], which is a silica matrix composite adopted for its variable reflectivity (i.e., thermal spectrum reflectivity equal to 0.2 and solar spectrum reflectivity equal to 0.8 [32]), and resistance to high temperatures (i.e., melting point above 1200 °C [16]). Middle layer is made of

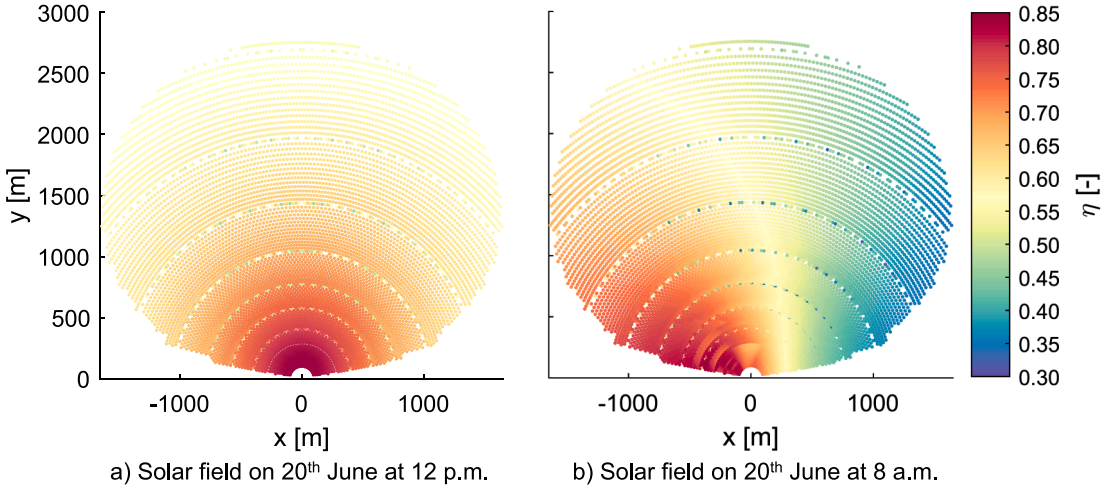

Fig. 9. Solar field layout, and heliostats' efficiency not considering intercept factor.

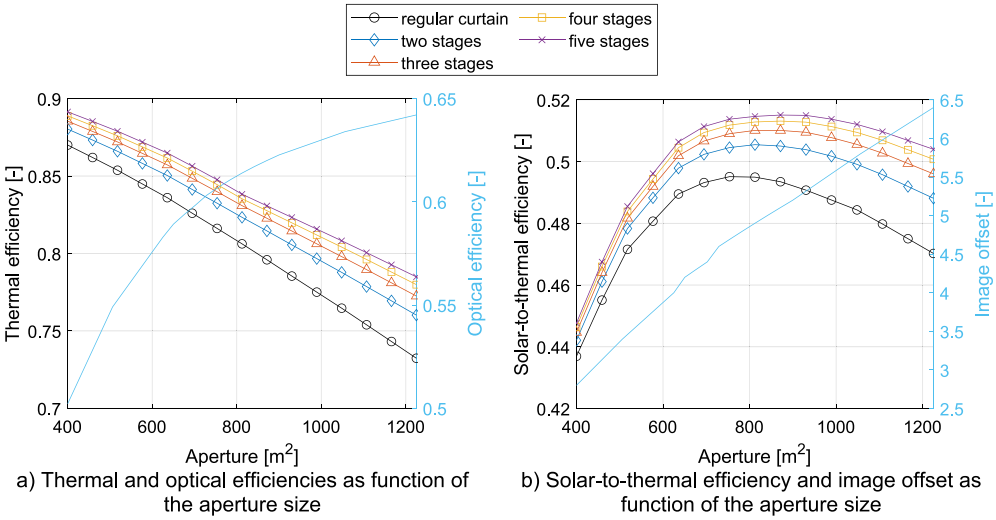

Fig. 10. On-design results of the different configurations considered.

Table 4
Design conditions of the different optimized configurations.

	Regular curtain	Two stages	Three stages	Four stages	Five stages
Design aperture area	784 m^2	812.25 m^2	841 m^2	870.25 m^2	870.25 m^2
Design aperture height	28 m	28.5 m	29 m	29.5 m	29.5 m
$\dot{Q}_{in,rec,nom}$	723 MW	727 MW	731 MW	734 MW	734 MW
Maximum heat flux	1.972 MW/m^2	1.961 MW/m^2	1.951 MW/m^2	1.934 MW/m^2	1.934 MW/m^2
Design intercept efficiency	92.3 %	92.8 %	93.3 %	93.7 %	93.7 %
Design optical efficiency	61.1 %	61.4 %	61.7 %	62.0 %	62.0 %
Design thermal efficiency	81.1 %	82.3 %	82.7 %	82.8 %	83.1 %
Design solar-to-thermal efficiency	49.5 %	50.6 %	51.0 %	51.3 %	51.5 %

Microtherm micro-porous insulation [33]. Finally, outer layer that is in contact with the ambient is made of HD board as it is relatively cheap and has good thermal properties (i.e., thermal conductivity of 0.14 W/mK at 650 °C) [16].

In the yearly analysis, round-trip efficiency of the TES is adopted to be 99 %, and its size is assumed equal to 12.5 h, as range of 10–15 h is provided in [3]. PB adopts a re-compressed sCO_2 cycle with a maximum temperature, recommended by [3], of 700 °C. Performance of the PB as function of the ambient temperature is taken from Alfani et al. [14]. Nominal net electric power output is assumed equal to 100 MW_{el} at design conditions (ambient temperature of 35 °C). This results in a nominal thermal power input equal to 217 MW_{th}, and a nominal net electric efficiency of 46.0 %. It is assumed that the fans of the heat rejection unit are controlled to keep the thermodynamic cycle unchanged regardless of the ambient temperature, thus power input to the cycle is always the same. However, the value of the net electric efficiency decreases when the ambient temperature increases, and thus net electric power output decreases, because of the increased fans consumption.

Lastly, control volume grid for the irradiated part of the curtain is adopted based on the results of a sensitivity analysis. Adopted grid is 60×60 as its deviation with respect to the 100×100 case for all the configurations considered is below 1 %, while reducing significantly computational time. Number of control volumes in the width direction is also 60 for both the part above and below the irradiated one. Meanwhile, number of control volumes in the vertical direction for those parts is chosen keeping the height of the control volume similar to that of the irradiated part, but slightly lower, to have integer number of control volumes and respect the physical size of the system.

5. Results

In this section on-design sizing results of different receiver configurations are shown. This is followed by the considerations regarding the thermal model outcomes at design conditions. Finally, results of the off-design and yearly performance analysis are presented.

5.1. On-design results

For all the configurations considered (see Fig. 8), the methodology explained in Section 2.2.2 is employed considering the plant characteristics described in Section 4 and varying the receiver aperture from 400 m^2 (20×20 m) to 1225 m^2 (35×35 m). Maximum flux that the inner layer of the back wall, RSLE-57, can withstand is equal to 2 MW/m^2 [16], therefore this value of flux is assumed as the constraint for the aiming strategy, to operate the receiver in a safely manner and to avoid overestimating the receiver optical performance by reducing spillage losses. However, please note that, in reality, it can be possible to increase this flux limit even further as the particles can be directly irradiated almost without consequence.

Fig. 10 represents efficiencies of all considered configurations, as well as the value of image offset adopted for the aiming strategy. Moreover, Table 4 reports the final design conditions. Thermal efficiency decreases with increasing the size, as both radiative and advective losses increase. On the other side, optical efficiency increases as bigger receiver reduces spillage losses. Therefore, as one efficiency increases and the other decreases, product of these two efficiencies, called "solar-to-thermal efficiency", must have a maximum. This maximum increases with the number of stages due to lower advective losses, as the fall height of each stage decreases with increasing the number of them. Moreover, it is possible to notice that the optimum is moving towards larger curtains while increasing the number of stages.

Image offset also increases with size, as bigger receivers allow to concentrate solar power more towards the centre without violating the peak flux constraint. Finally, design thermal efficiency increases with increasing the number of stages, and it is between 81 % and 83 %, thus not being able to reach SunShot target of 90 % [3]. The effect of adopting different aspect ratios (ratio of aperture height over width) for the aperture is evaluated for the optimal size of the regular curtain aperture. It is varied between 0.5 and 2.0 with the step of 0.25, and only value of 0.75 provides better performance compared to the value of 1.0, which is adopted for the simulations in Fig. 10. However, this increase in performance is limited (0.75 provides solar-to-thermal efficiency of 49.6 % compared to 49.5 % for the aspect ratio of 1.0), thus it is decided to keep the aspect ratio equal to 1.0 for all the configurations. Same analysis is also carried out for the five stages configuration, and as in the case of the regular curtain only aspect ratio of 0.75 provides limited increase in performance (0.75 provides solar-to-thermal efficiency of 51.6 % compared to 51.5 % for the aspect ratio of 1.0). It is worth noting that the accuracy of the sensitivity analyses performed on the aspect ratio are affected by the simplified method adopted for the advective loss assessment; indeed, advective loss model was developed for square apertures and might need adjustment for other aspect ratios where buoyancy effects would have more of an impact.

To understand if the assumption of ideal mixing, which is adopted for the multistage configurations, is valid, it is necessary to study the no mixing case. No mixing means that the presence of troughs does not affect the temperature profile, they just restart the curtain in terms of particle velocity, particle volume fraction, and curtain thickness. Since the two cases are the extreme ones, the actual efficiency of the multi-stage configuration should be a value in between those two.

Five stages configuration is investigated, being the best one from the performance point of view, and its on-design condition is simulated assuming no mixing inside the troughs. The thermal efficiency value with no mixing is 83.0 %, compared to 83.1 % with ideal mixing. Given the negligible impact of this assumption on the thermal efficiency of the receiver, further analyses will be based on the ideal mixing assumption.

In Fig. 12 are shown the trends, considering aperture size equal to 29.5x29.5 m, for the particle temperature, particle velocity, particle volume fraction, and curtain reflectivity. Considered sun position corresponds to solar noon on 20th June, and the heat flux on the particle curtain is reported in Fig. 11.

For the sake of brevity, only the trends for the regular curtain and five stages are shown, assuming both ideal and no mixing for the last one. Regarding the optical properties, only reflectivity is shown because the transmissivity is negligible under design conditions (at the start of the curtain transmissivity is around 10^{-74} while at the end of the curtain it is around 10^{-18}) and thus the reflectivity is enough to fully describe all the optical properties trends.

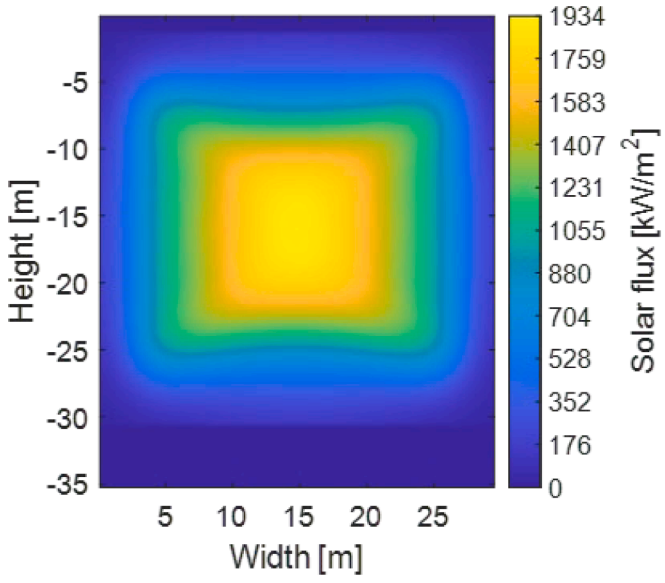

Fig. 11. Heat flux on the particle curtain, considering aperture size equal to 29.5 × 29.5 m.

Since the reflectivity trends have the same shape as the volume fraction ones (the reason will be explained later) its trends are shown with an overlayed contour to the volume fraction figures.

Regarding the temperature distribution for the regular curtain, its value is ranging a lot along the width ($\Delta T > 200\,^{\circ}C$) because of the concentrated heat flux adopted. Instead, for the five stages with ideal mixing assumption this variation is mitigated because of the uniform temperature at the end of each trough, while for the no mixing case the trend is practically equal to the one of the regular curtain.

The particle temperature trend affects also other variables such as velocity, indeed, the higher the temperature, the higher is the drag force effect because air dynamic viscosity increases and air density decreases (see Eq. (3)); since the temperature increases along the fall, a slight deceleration of particles can be observed. The reason behind the particle deceleration is related to the concept of terminal velocity: after a few meters the terminal velocity is reached, and if the temperature would have remained constant the velocity profile would have reached a plateau. However, as the particle temperature increases along the falling coordinate, increasing the drag force, particle velocity decreases instead of remaining constant. It should be noted that, for the sake of easier interpretation of the velocity figures, colour axis is starting from 3 m/s even though velocity after each trough is restarted to the starting velocity evaluated by Eq. (16). Experimental analyses are recommended to verify the validity of the obtained results, because the terminal velocity of the particles is probably underestimated due to the results obtained from the analytical drag model adopted in this work, since in [19] experiments with measured particle velocities above 5 m/s are reported. However, please note that the analytical drag model in the same reference provided similar values of the terminal velocity to those obtained in this work.

Regarding the volume fraction, its value is high just in the first meter of the fall and then it suddenly moves towards low values (<0.1) once the thickness of the curtain increases; in the five stages configuration the curtain is continuously restarted and thus the volume fraction shows peaks with high values after the curtain is restarted. Please note that, as the value of volume fraction decreases rapidly during particles' fall, there is no significant difference in its value in the case of free-falling particle curtain and curtain with five stages, except in the areas where the curtain is restarted.

Finally, it is worthy to mention that the reflectivity follows the same trend as the particle volume fraction. This comes from the optical properties model described in [28] in which reflectivity depends on the volume fraction. Particle curtain proves to be more reflective with higher values of volume fraction because, the denser the curtain, the more difficult it is for solar rays to reach all the layers and be absorbed.

5.2. Off-design performance

Performance of the different configurations under off-design conditions is evaluated using the approach explained in Section 2.2.3, by varying the DNI from 110 % of its design value (1000 W/m^2) to the minimum one that permits the receiver to operate. To find out the minimum thermal input, the thermal model is simulated decreasing the DNI down to the value that does not give results, as the thermal power absorbed is not enough for reaching the desired particle outlet temperature.

Simulations' results show that the thermal efficiency from the model does not depend on the heat flux distribution, but only on the power incident on the receiver. For more details, refer to Appendix D.

Fig. 13 clearly shows that adoption of the multistage configuration is

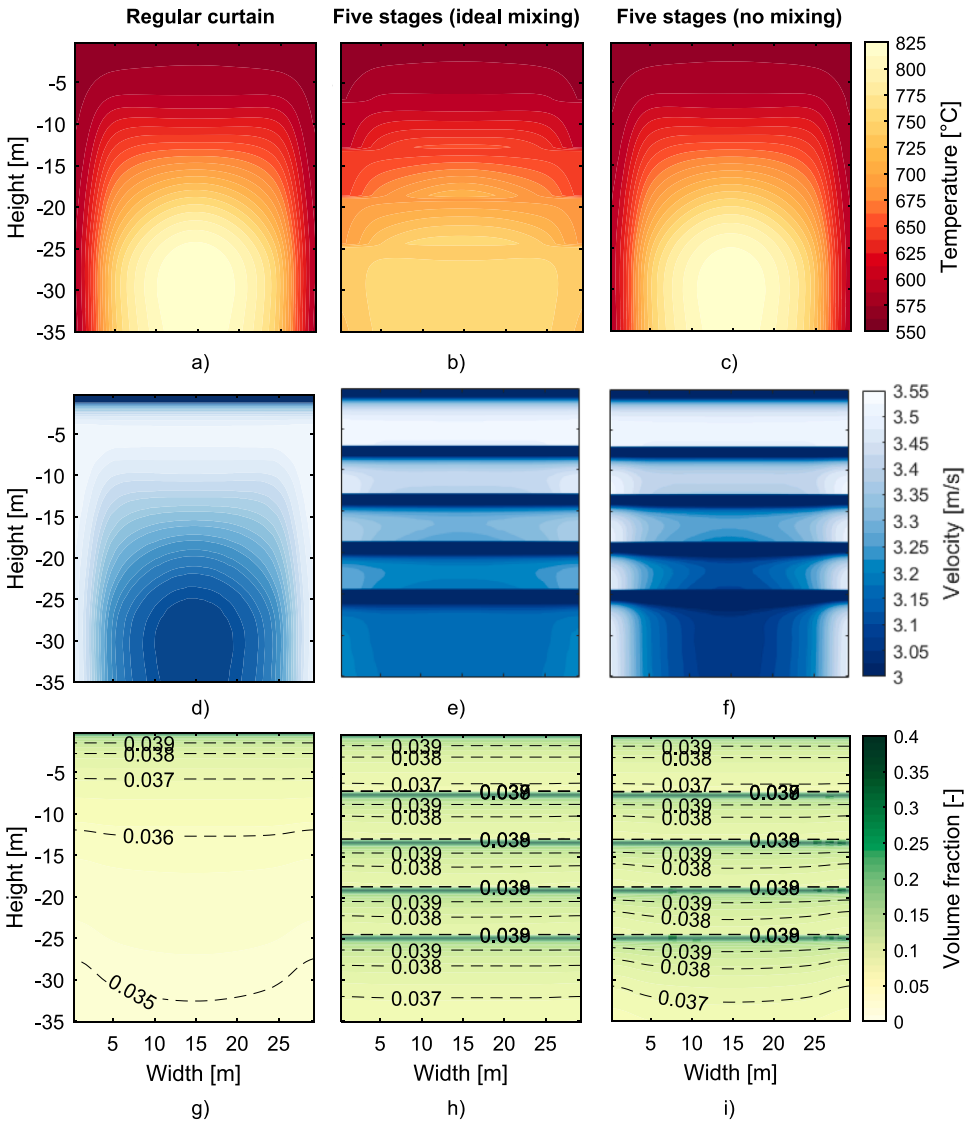

Fig. 12. Thermal model results under design conditions for the regular curtain and five stages curtain both with ideal mixing and no mixing: first six figures are showing the particle temperature (a–c) and the particle velocity (d–f), while the last three (g–i) show the particle volume fraction with the colour gradient and curtain reflectivity with overlayed contours.

always beneficial in terms of efficiency, with even higher efficiency gains at low power input because frequent restarting of the particle curtain significantly improves its opacity.

Adoption of the recirculation does not seem to be as beneficial as the multistage, but anyway it permits to enlarge the operating range of the receiver. For the sake of clarity, only the off-design curve of five stages configuration is shown among the multistage ones.

Regarding the operating range, five stages configuration requires a minimum incident power of 153 MW and proves to be the best configuration, while recirculation and regular curtain require 155 MW and 181 MW, respectively.

5.3. Yearly performance analysis

Based on the receiver performance as function of the input solar power (Fig. 13) the yearly performance analysis can be carried out, following the methodology explained in Section 2.2.4.

To visualize the switching principle of the recirculation concept, Fig. 14 shows the so called "net" thermal efficiency curves of both the regular curtain and recirculation case. These curves are made in a simplified manner by considering PB efficiency to be constant and equal to the nominal one, just to convert electric consumption of the elevator into thermal energy. This thermal energy is then subtracted from the thermal energy produced by the receiver, and new thermal efficiency called "net" thermal efficiency is calculated. Red dot in Fig. 14 illustrates the point below which it is more convenient to adopt recirculation. It should be noted that in the yearly performance analysis actual point of switching is determined hour-by-hour depending on the PB efficiency at that specific condition.

Results of the yearly performance analysis are reported in Table 5 and Table 6. They are reported only for the regular curtain, recirculation and five stages because other multistage configurations provide similar but lower performance than the five stages one. "Defocusing" refers to the loss of solar energy because mirrors need to be defocused as TES is full.

Optical efficiency is the same for the regular curtain and recirculation as they use exactly the same receiver; on the other hand, five stages configuration has higher optical efficiency because receiver is larger, thus reducing spillage losses. Regarding the thermal efficiency, recirculation provides higher values with respect to the regular curtain, which is expected as its aim is to increase performance at part load conditions; however, this increase in performance is limited (yearly

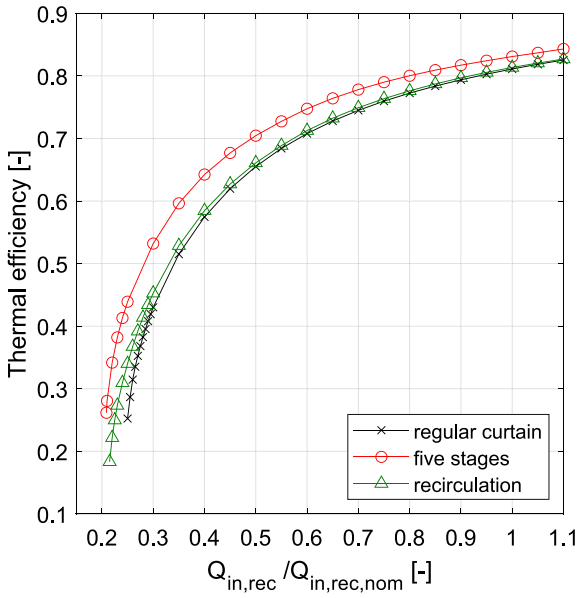

Fig. 13. Off-design performance curves of the regular curtain, recirculation and five stages.

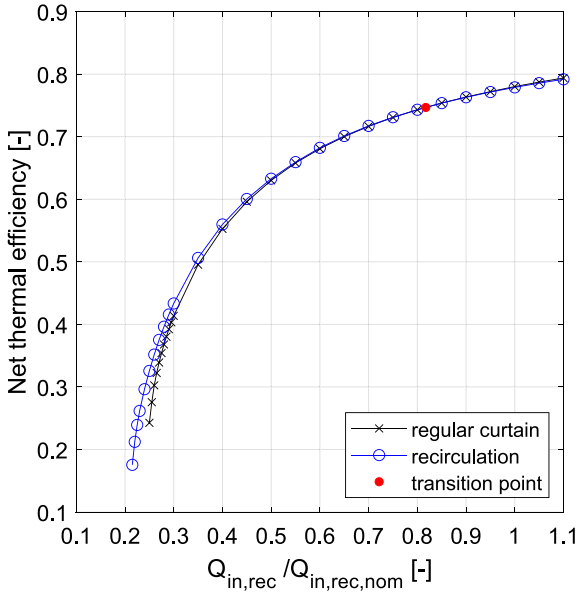

Fig. 14. "Net" thermal efficiency curves for the regular curtain and recirculation.

Table 5
Yearly efficiencies of the regular curtain, recirculation and five stages.

	Regular curtain	Recirculation	Five stages
Yearly defocusing efficiency	99.5 %	99.5 %	98.7 %
Yearly optical efficiency	55.5 %	55.5 %	56.4 %
Yearly thermal efficiency	72.0 %	72.5 %	75.3 %
Yearly TES efficiency	99.5 %	99.5 %	99.5 %
Yearly PB net cycle efficiency	46.2 %	46.2 %	46.2 %
Yearly auxiliary efficiency	96.2 %	96.0 %	96.1 %
Yearly overall efficiency	17.6 %	17.7 %	18.5 %

thermal efficiency is increased only by 0.5 %). Highest value of thermal efficiency is obtained for the five stages configuration, which is mainly driven by lower advective losses. Regarding the auxiliary efficiency, recirculation is the worst case as it has electricity consumption

Table 6
Yearly energy performance of the regular curtain, recirculation and five stages.

	Regular curtain	Recirculation	Five stages
Energy incident on the field (GWh)	3226	3226	3226
Energy incident on the field without energy lost due to defocusing (GWh)	3209	3208	3182
Energy incident on the receiver (GWh)	1781	1780	1795
Energy absorbed by the particles (GWh)	1282	1290	1351
Energy absorbed by the PB (GWh)	1276	1284	1344
Gross electric energy produced (GWh)	590	593	621
Net electric energy produced (GWh)	567	570	597
Equivalent hours (h)	5671	5696	5973
Capacity factor (%)	64.7	65.0	68.2

associated with the additional elevator. Finally, as the energy yield of the recirculation case is only slightly higher than the regular curtain one, its adoption could not be justified because of the additional costs and complexity associated.

6. Conclusions

In this work a thermal model was developed to assess performance of falling particle receivers for solar tower plants. The model was implemented in MATLAB® starting from the model described by González-Portillo et al. [11]. Overview of the main differences between base model and developed one are reported in Table 7.

Firstly, the model described in [11] was replicated and successfully verified. Next, particles' velocity trends obtained accounting for the drag force effect were verified against experimental data from Hruby et al. [18] and the implemented model results showed good agreement with the experimental ones at high temperature. Then, thermal model was verified against CFD simulation reported in Mills et al. [29]. Results showed that model developed in this work provides better agreement compared to the starting model from [11] (i.e., thermal efficiency absolute error of 0.8 % against 1.0 %), and that the consideration of drag force is beneficial for the model accuracy.

The developed receiver thermal model was applied to a specific case study. In detail, free-falling particle and multistage receivers with different number of troughs were investigated considering a solar field similar to the one described in Mehos et al. [3], located in Daggett, California (34.86609, −116.88806) and designed to feed a 100 MW_{el} sCO_2 power cycle.

For each investigated configuration, the aperture size was determined by maximizing the solar-to-thermal efficiency. For each size the heliostats' aiming strategy was set to obtain a maximum heat flux of 2 MW/m^2. Results showed that the optimal receiver size increases with increasing the number of stages. Regular curtain had an aperture size equal to 28x28 m with a solar-to-thermal efficiency equal to 49.5 %. On the other hand, aperture size was equal to 29.5 × 29.5 m for the five

Table 7
Overview of main differences between base and improved model.

	Base model [11]	Improved model (This work)
Particle curtain discretization	1D	2D
Back wall discretization	1D	3D
Drag force effect	No	Yes
Back wall reflectivity as function of wavelength	No	Yes
Particle specific heat as function of temperature	No	Yes
Correlation for evaluating convective heat transfer coefficient	No	Yes
Different value of view factor for different curtain parts	No	Yes
View factor correction for improving curtain-cavity interaction	No	Yes

stages with a solar-to-thermal efficiency of 51.5 %.

Using the optimal configuration obtained during on-design, off-design analysis as well as yearly performance analysis, which takes into account presence of the TES and the PB, were performed for all investigated cases, and results showed that the performance improves with the number of stages; indeed, five stages configuration provided highest thermal efficiencies (i.e., 75.3 %), as well as the highest solar-to-electric efficiency (i.e., 18.5 % vs 17.6 % for the regular curtain), among all the configurations. For the regular curtain the option of recirculation was also considered with the aim of increasing the thermal efficiency under part load conditions, and also to extend the operating range of the receiver. However, the increase of the energy yield using recirculation is only marginal (i.e., net electric energy produced of 570 GWh vs 567 GWh for the regular curtain), and probably does not justify the increase in CAPEX (e.g., the cost of the additional elevator) and OPEX (more complicated operation due to switching).

The developed model shows a good flexibility for performing different kinds of analyses. Indeed, it can be adapted to change the working principle of the curtain itself or its configuration (e.g., adoption of multistage configurations or recirculation), moreover it can work with any type and size of particles by just changing their properties in the model inputs.

Further improvements to the model that could be considered in future works might be: i) the development of an advective heat transfer coefficient correlation based on curtain local velocities, ii) the implementation of procedures to account for wind effect on the receiver performance, also taking into account particle loss, or iii) a more detailed analysis of troughs used in the multistage particle receivers that accounts for particle mixing and thermal losses.

CRediT authorship contribution statement

Omar Pasqualotto: Conceptualization, Methodology, Software, Validation, Data curation, Writing – original draft. **Filip Sobic:** Conceptualization, Methodology, Software, Validation, Data curation, Writing – original draft. **Giancarlo Gentile:** Conceptualization, Methodology, Software, Writing – review & editing. **Marco Binotti:** Conceptualization, Writing – review & editing. **Andrea Giostri:** Conceptualization, Writing – review & editing. **Giampaolo Manzolini:** Conceptualization, Supervision, Writing – review & editing, Funding acquisition.

Declaration of Competing Interest

The authors declare that they have no known competing financial interests or personal relationships that could have appeared to influence the work reported in this paper.

Appendix A. – Sensitivity analyses

Sensitivity analysis on the particle and air velocity ratio is performed by simulating the optimal size free-falling particle receiver at design conditions and varying the velocity ratio from 0.3 to 0.9 with step of 0.1. Then, results are reported in terms of deviation of thermal efficiency with respect to the case with velocity ratio of 0.6. Another sensitivity analysis is performed to assess the impact of advective heat transfer coefficient h_{adv} on receiver efficiency. The optimal size free-falling particle receiver is simulated at design condition by assuming advective heat transfer coefficient equal to 0.5, 0.75, 1.25, and 1.5 of its nominal value. Results are represented in terms of deviation of receiver thermal efficiency with respect to the receiver thermal efficiency with nominal value of h_{adv}.

As it can be seen from Fig. A1, influence of the ratio of particle and air velocity on the thermal efficiency of the receiver is negligible as the biggest deviation is only 0.15 %. Therefore, assuming the value of 0.6 in Section 2.1.1 can be considered justified. On the other hand, the advective heat transfer coefficient has much stronger impact on the receiver thermal efficiency. However, a change of h_{adv} by 50 % leads to change in the thermal efficiency of only 6.2 %.

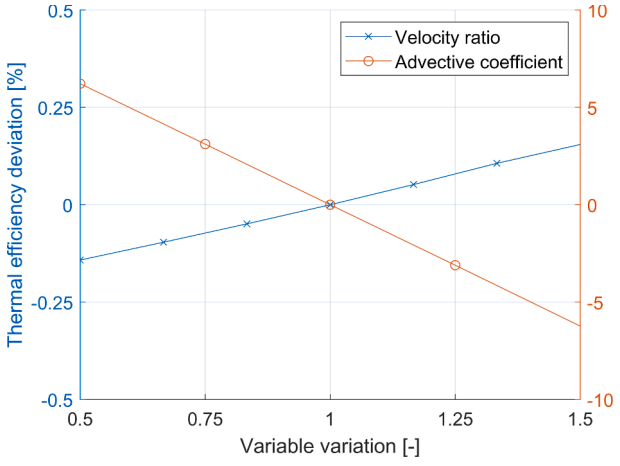

Fig. A1. Sensitivity analysis results.

Appendix B. – Drag force correction

Drag force correlations taking into account the particle volume fraction, reported in [34–36], are implemented, but neither of them provides better matching with experimental data than the one shown in Eq. (3), so they are not employed in the final version of the model. Hence, it is decided to investigate the approach suggested by Rusche and Issa [22] and use in the momentum balance equation a correction factor (a) that depends on the volume fraction. In [22], the correction factor (a) is used to multiply the drag coefficient of a single particle and thus obtain the value for the curtain by considering the effect of neighboring particles.

Even though the drag model implemented in this work already considers the particles as a part of the curtain, the adoption of a volume fraction dependent a is studied for improving the matching of velocity outcomes with experimental results. Function for evaluating the correction factor (a) is reported in Eq. (B1).

$$a = e^{K_1 \varphi_p} + {\varphi_p}^{K_2} \tag{B1}$$

Since in [22] the coefficients K_1 and K_2 are derived by fitting the experimental results obtained with particles in water, they cannot be used for the purpose of this work. Hence, the values of the coefficients K_1 and K_2 are derived through a least squares fitting procedure based on the experimental velocity data provided by Hruby et al. [18], and are equal to $1.393 \bullet 10^{-5}$ and 0.131, respectively.

Results of the drag model using a are reported in Fig. B1 against drag model results without correction, model reported by Hruby et al. [18], and experimental results reported by Hruby et al. [18]. Even though correction factor adoption provides better matching for the cases shown in Fig. B1b and c, the matching is worse for the case shown in Fig. B1a, that is the most representative of the actual receiver operation (i.e., it has higher temperature and mass flow rate). Moreover, the differences between the receiver thermal efficiencies evaluated with and without the correction factor are always negligible (relative deviation <0.05 %). Therefore, correction factor is not considered in the adopted model, and the value of a in Eq. (3) is set equal to one.

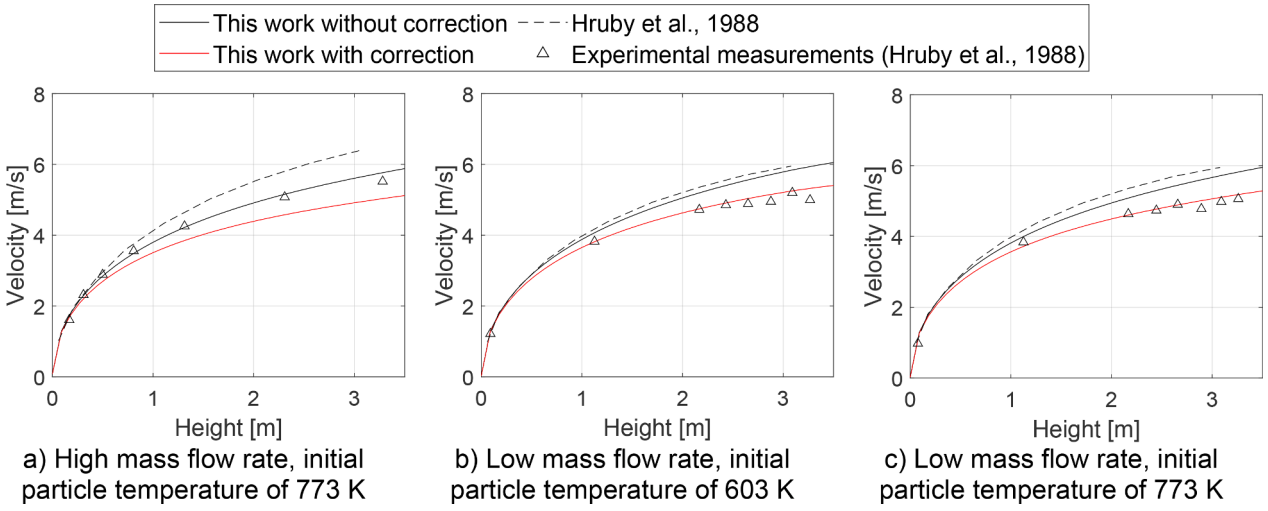

Fig. B1. Drag model with the correction factor results.

Appendix C. – Variable reflectivity

There is a term $\rho_c q_{w-c}$ in Eq. (12) accounting for both the solar and thermal radiation that cannot be multiplied neither with $\rho_{w,s}$ nor $\rho_{w,t}$. To consider the different reflectivity value depending on the wavelength also for this term, a weighted average is adopted to derive a weighted reflectivity $\rho_{w,w}$. The devised approach consists in predicting how much of the incoming radiation is in the thermal and solar spectrum in each control volume, and for each of them a value of $\rho_{w,w}$ is assessed. For this purpose, three terms are considered to be exchanged between the curtain and the back wall: $\tau_c q_{in,rec}$ is the one coming from the sun, while $\varepsilon_c \sigma T_p^4$ and $\varepsilon_w \sigma T_{i,j,cav-A}^4$ are the ones emitted by the curtain and the back wall, respectively. Then, multiple reflections of these terms between the curtain and the back wall are considered, two reflections against the back wall for $\tau_c q_{in,rec}$ and $\varepsilon_c \sigma T_p^4$, and one reflection for $\varepsilon_w \sigma T_{i,j,cav-A}^4$ (to be consistent with the number of passages). It is verified that the adoption of higher number of reflections is not necessary since the results in terms of reflectivity values do not change.

Described approach can be visualized in Fig. C1; for the sake of figure comprehension, only initial and final terms are explicitly shown (with arrows) while the others, that are still hitting the back wall in the previous reflections, are not reported. From this approach, Eqs. (C1)–(C3) are derived and used to assess the value of the weighted reflectivity.

$$q_{solar} = \tau_c q_{in,rec} \left[1 + \rho_{w,s}\rho_c \left(1 + \rho_{w,s}\rho_c\right)\right] \tag{C1}$$

$$q_{thermal} = \varepsilon_c \sigma T_p^4 \left[1 + \rho_{w,t}\rho_c \left(1 + \rho_{w,t}\rho_c\right)\right] + \varepsilon_w \sigma T_{i,j,cav-A}^4 \rho_c \left(1 + \rho_{w,t}\rho_c\right) \tag{C2}$$

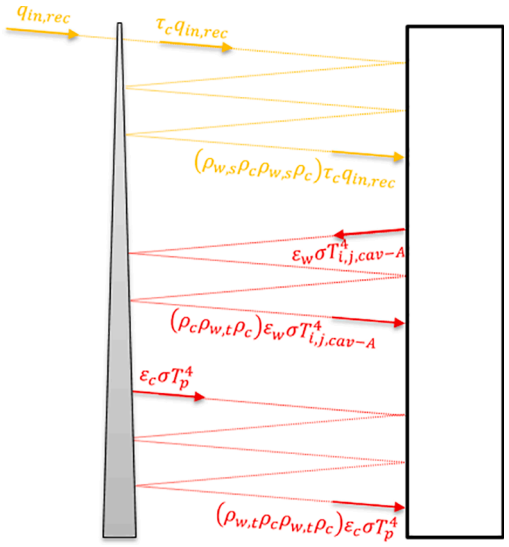

Fig. C1. Ray-following approach adopted for deriving the weighted reflectivity (solar radiative term and thermal radiative terms are shown in yellow and in red, respectively).

$$\rho_{w,w} = \frac{\rho_{w,s} q_{solar} + \rho_{w,t} q_{thermal}}{q_{solar} + q_{thermal}} \tag{C3}$$

Appendix D. – Heat flux map discussion

To investigate the impact of the heat flux map distribution on the off-design receiver thermal efficiency, regular curtain is simulated for different days and hours, and the resulting thermal efficiencies are plotted in Fig. D1 against the ratio between the thermal power input into the receiver and the nominal thermal power input into the receiver.

It is possible to notice that simulations' results exhibit the same trend; hence, the thermal efficiency from the model does not depend on the sun position, but only on the power incident on the receiver.

For the sake of completeness, Fig. D2 reports heat flux maps for the regular curtain under nominal conditions on June 20th at 12p.m. and on December 20th at 8 a.m. Heat flux maps are not reported for other conditions since the flux distribution does not change by changing the thermal input.

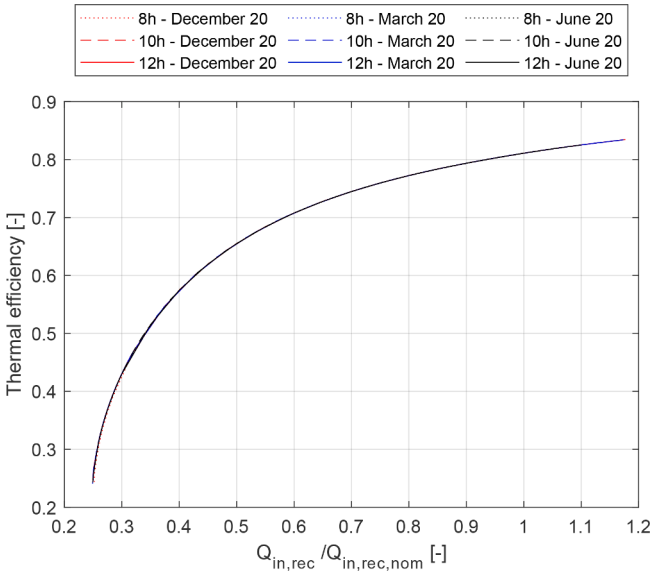

Fig. D1. Regular curtain off-design performance for different days and hours.

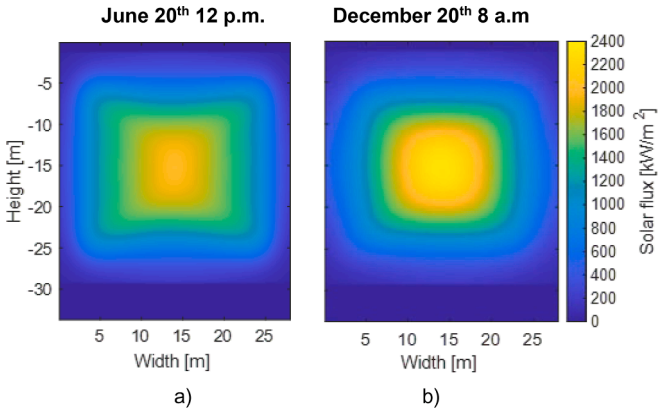

Fig. D2. Heat flux maps on the particle curtain under nominal thermal input, on June 20th at 12p.m. (a) and on December 20th at 8 a.m. (b).

References

[1] T. Bruckner et al., "2014: Energy Systems," in Climate Change 2014: Mitigation of Climate Change. Contribution of Working Group III to the Fifth Assessment Report of the Intergovernmental Panel on Climate Change, O. Edenhofer, R. Pichs-Madruga, Y. Sokona, E. Farahani, S. Kadner, K. Seyboth, A. Adler, I. Baum, S. Brunner, P. Eickemeier, B. Kriemann, J. Savolainen, S. Schlömer, C. von Stechow, T. Zwickel, and J. C. Minx, Eds. Cambridge University Press, 2014, p. 1465.

[2] International Energy Agency, "Net Zero by 2050: A Roadmap for the Global Energy Sector," Int. Energy Agency, 2021.

[3] M. Mehos et al., "Concentrating Solar Power Gen3 Demonstration Roadmap," 2017. doi: 10.2172/1338899.

[4] United States Department of Energy, "2030 Solar Cost Targets," 2021.

[5] United States Department of Energy, "Generation 3 Concentrating Solar Power Systems (Gen3 CSP) Phase 3 Project Selection," 2021.

[6] C.K. Ho, A review of high-temperature particle receivers for concentrating solar power, Appl. Therm. Eng. 109 (2016) 958–969.

[7] R. Jiang, M.-J. Li, W.-Q. Wang, X.-D. Xue, D. Li, A new methodology of thermal performance improvement and numerical analysis of free-falling particle receiver, Sol. Energy 230 (2021) 1141–1155.

[8] N.P. Siegel, C.K. Ho, S.S. Khalsa, G.J. Kolb, Development and evaluation of a prototype solid particle receiver: on-sun testing and model validation, J. Sol. Energy Eng. Trans. ASME 132 (2010), https://doi.org/10.1115/1.4001146.

[9] W. Wang, Y. Shuai, B. Guene Lougou, B. Jiang, Thermal performance analysis of free-falling solar particle receiver and heat transfer modelling of multiple particles, Appl. Therm. Eng. 187 (2021) 116567.

[10] M. Röger, L. Amsbeck, B. Gobereit, R. Buck, Face-down solid particle receiver using recirculation, J. Sol. Energy Eng. Trans. ASME 133 (2011), https://doi.org/10.1115/1.400426.

[11] L.F. González-Portillo, K. Albrecht, C.K. Ho, Techno-economic optimization of CSP plants with free-falling particle receivers, Entropy 23 (1) (2021) 76.

[12] L.F. González-Portillo, V. Soria-Alcaide, K. Albrecht, C.K. Ho, B. Mills, Benchmark and analysis of a particle receiver 1D model, Sol. Energy 255 (2023) 301–313.

[13] M.J. Wagner, T. Wendelin, SolarPILOT: A power tower solar field layout and characterization tool, Sol. Energy 171 (Sep. 2018) 185–196, https://doi.org/10.1016/J.SOLENER.2018.06.063.

[14] D. Alfani, M. Astolfi, M. Binotti, P. Silva, E. Macchi, Off-design performance of CSP plant based on supercritical CO2 cycles, AIP Conf. Proc. 2303 (2020), https://doi.org/10.1063/5.0029801.

[15] B. Mills, C.K. Ho, Simulation and performance evaluation of on-sun particle receiver tests, in AIP Conference Proceedings, 2019, vol. 2126. doi: 10.1063/1.5117548.

[16] J. Christian, C. Ho, Design requirements, challenges, and solutions for high-temperature falling particle receivers, in: AIP Conference Proceedings, 2016, vol. 1734. doi: 10.1063/1.4949060.

[17] S.S.S. Khalsa et al., "CFD simulation and performance analysis of alternative designs for high-temperature solid particle receivers," in ASME 2011 5th International Conference on Energy Sustainability, ES 2011, 2011, no. PARTS A, B, AND C. doi: 10.1115/ES2011-54430.

[18] J. Hruby, R. Steeper, G. Evans, C. Crowe, An experimental and numerical study of flow and convective heat transfer in a freely falling curtain of particles, J. Fluids Eng. Trans. ASME 110 (2) (1988) 172–181.

[19] C.K. Ho, J.M. Christian, D. Romano, J. Yellowhair, N. Siegel, L. Savoldi, R. Zanino, Characterization of particle flow in a free-falling solar particle receiver, J. Sol. Energy Eng. Trans. ASME 139 (2017), https://doi.org/10.1115/1.4035258.

[20] K. Kim, N. Siegel, G. Kolb, V. Rangaswamy, S.F. Moujaes, A study of solid particle flow characterization in solar particle receiver, Sol. Energy 83 (10) (2009) 1784–1793.

[21] D. Dodds, A.R. Sarhan, J. Naser, Experimental and numerical study of drag forces on particles in clusters, Powder Technol. 371 (2020) 195–208.

[22] H. Rusche, R.I. Issa, The effect of voidage on the drag force on particles, droplets and bubbles in dispersed two-phase flow, Proc. Japanese Eur. Two-Phase Flow Meet, 1, 2000.

[23] M. Kanitz, J. Grabe, The influence of the void fraction on the particle migration: A coupled computational fluid dynamics–discrete element method study about drag force correlations, Num. Anal. Meth. Geomech. 45 (1) (2021) 45–63.

[24] N. Lauzier, "View Factors (https://www.mathworks.com/matlabcentral/fileexchange/5664-view-factors), MATLAB Central File Exchange," 2022.

[25] D.L. Siebers, J.S. Kraabel, Estimating convective energy losses from solar central receivers, Sandia Rep. (1984). SAND-84-8717.

[26] G. Gentile, G. Picotti, M. Binotti, M.E. Cholette, G. Manzolini, Dynamic thermal analysis and creep-fatigue lifetime assessment of solar tower external receivers, Sol. Energy 247 (Nov. 2022) 408–431, https://doi.org/10.1016/j.solener.2022.10.010.

[27] G. Gentile, G. Picotti, F. Casella, M. Binotti, M.E. Cholette, G. Manzolini, SolarReceiver2D: a modelica package for dynamic thermal modelling of central receiver systems, IFAC-PapersOnLine 55 (20) (Jan. 2022) 259–264, https://doi.org/10.1016/J.IFACOL.2022.09.105.

[28] L.F. González-Portillo, R. Abbas, K. Albrecht, C. Ho, Analysis of optical properties in particle curtains, Sol. Energy 213 (2021) 211–224.

[29] B. Mills, B. Schroeder, L. Yue, R. Shaeffer, C.K. Ho, Optimizing a falling particle receiver geometry using CFD simulations to maximize the thermal efficiency, AIP Conf. Proc. 2303 (2020), https://doi.org/10.1063/5.0029331.

[30] B.H. Mills, C.K. Ho, N.R. Schroeder, R. Shaeffer, H.F. Laubscher, K.J. Albrecht, Design evaluation of a next-generation high-temperature particle receiver for concentrating solar thermal applications, Energies 15 (5) 2022. doi: 10.3390/en15051657.

[31] I. ZIRCAR Refractory Composites, "Silica Composites," 2005.

[32] J. Christian, C. Ho, W. Kolb, J. Kelton, D. Ray, Design and evaluation of an on-sun prototype falling-particle cavity receiver, in: ASME 2014 8th International Conference on Energy Sustainability, ES 2014 Collocated with the ASME 2014 12th International Conference on Fuel Cell Science, Engineering and Technology, 2014, vol. 1. doi: 10.1115/ES2014-6446.

[33] Promat, "Microtherm Panel," 2017.

[34] A. Pidaparthi, W. Landman, J. Hoffmann, F. Dinter, Optical performance considerations for analysis and simulation of power tower plants, AIP Conf. Proc. 1850 (2017), https://doi.org/10.1063/1.4984555.

[35] L. Schiller, Z. Naumann, A drag coefficient correlation, 77, 13–14. 1935. doi: 10.1016/j.ijheatmasstransfer.2009.02.006.

[36] R. Di Felice, The voidage function for fluid-particle interaction systems, Int. J. Multiph. Flow 20 (1) (1994) 153–159.